Research Article

<*Grin1*$^{Y647S/+}$ Mice: A Preclinical Model of *GRIN1*-Related Neurodevelopmental Disorder>

<Megan T. Sullivan BSc [1], Patrick Tidball PhD [2,3], Yuanye Yan BSc [1], Katheron Intson PhD [1], Wenjuan Chen MD PhD [4,5], Yuchen Xu MD PhD [4,6], Sridevi Venkatesan PhD [7], Wendy Horsfall MSc [1], John Georgiou PhD [2,3], Peter S.B. Finnie PhD [1], Evelyn K. Lambe PhD [7], Stephen F. Traynelis PhD [4,8,9], Ali Salahpour PhD [1], Hongjie Yuan MD PhD [4,8,] Graham L. Collingridge PhD [2,3,7], Amy J. Ramsey PhD[1].

<From the [1]Department of Pharmacology & Toxicology, University of Toronto, Toronto, ON, Canada; [2]Lunenfeld-Tanenbaum Research Institute, Mount Sinai Hospital, Sinai Health System, Toronto, ON, Canada; [3]TANZ Centre for Research in Neurodegenerative Diseases, University of Toronto, Toronto, ON, Canada; [4]Department of Pharmacology & Chemical Biology, Emory University School of Medicine, GA, USA; [5]Department of Psychiatry, Sir Run Run Shaw Hospital, Zhejiang University School of Medicine, Hangzhou, China; [6]Department of Neurology, the First Hospital of Wenzhou Medical University, Wenzhou, Zhejiang, 325000, China; [7]Department of Physiology, University of Toronto, Toronto, ON, Canada; [8]Center for Functional Evaluation of Rare Variants (CFERV), Emory University School of Medicine, GA, USA; [9]Emory Neurodegenerative Disease Center, Emory University School of Medicine, Atlanta, GA, USA. >

Corresponding author: Dr. Amy J. Ramsey
Corresponding author's address: PO Box 153, University of Toronto, 10th Floor, 777 Bay Street, Toronto, ON M5G2C8
Corresponding author's phone and fax: (416) 978-2509
Corresponding author's e-mail address: a.ramsey@utoronto.ca

ABSTRACT

Objective: *GRIN1*-related neurodevelopmental disorder (*GRIN1*-NDD) is characterized by clinically significant variation in the *GRIN1* gene, which encodes the obligatory GluN1 subunit of N-methyl-D-aspartate receptors (NMDARs). The identified p.Tyr647Ser (Y647S) variant — carried by a 33-year-old female with seizures and intellectual disability — is located in the M3 helix in the GluN1 transmembrane domain. This study builds upon initial *in vitro* investigations of the functional impacts of the *GRIN1* Y647S variant and examines its *in vivo* consequences in a mouse model.

Methods: To investigate *in vitro* functional impacts of NMDARs containing GluN1-Y647S variant subunits, GluN1-Y647S was co-expressed with wildtype GluN2A or GluN2B subunits in *Xenopus laevis* oocytes and HEK cells. *Grin1*$^{Y647S/+}$ mice were created by CRISPR-Cas9 endonuclease-mediated transgenesis and the molecular, electrophysiological, and behavioural consequences of the variant were examined.

Results: *In vitro*, NMDARs containing GluN1-Y647S show altered sensitivity to endogenous agonists and negative allosteric modulators, and reduced cell surface trafficking. *Grin1*$^{Y647S/+}$ mice displayed a reduction in whole brain GluN1 levels and deficiency in NMDAR-mediated synaptic transmission in the hippocampus. Behaviourally, *Grin1*$^{Y647S/+}$ mice exhibited spontaneous seizures, altered vocalizations, muscle strength, sociability, and problem-solving.

Interpretation: The Y647S variant confers a complex *in vivo* phenotype, which reflects largely diminished properties of NMDAR function. As a result, *Grin1*$^{Y647S/+}$ mice display atypical behaviour in domains relevant to the clinical characteristics of *GRIN1*-NDD and the individual carrying the variant. Ultimately, the characterization of *Grin1*$^{Y647S/+}$ mice accomplished in the present work expands our understanding of the mechanisms underlying *GRIN1*-NDD and provides a foundation for the development of novel therapeutics.

INTRODUCTION

GRIN-related neurodevelopmental disorder (*GRIN*-NDD) is characterized by clinically significant variation in genes coding for the subunits of the N-methyl-D-aspartate receptor (NMDAR) [1,2,3]. The *GRIN1* gene encodes the obligatory GluN1 subunit [4], which is required for proper function of all NMDARs [5,6,7]. NMDARs flux calcium when activated by concurrent occupation of glycine and glutamate sites on the GluN1 and GluN2 subunits, respectively, together with membrane depolarization [6,8,9]. These receptors are crucial to cognitive processes like learning and memory through mediation of brain plasticity [10,11].

GRIN1 variants can be familial in origin but are typically *de novo* missense variants [3]. With fewer than 100 published cases, the prevalence of *GRIN1*-related neurodevelopmental disorder (*GRIN1*-NDD) in the general population has yet to be established [3], but is estimated to be ~5 per 100,000 births [12]. These patients have a wide range of symptoms of varying severity. Nearly all present with some form of developmental delay, atypical cognition, and intellectual disability, while two thirds of patients present with epilepsy, stereotyped movements, and abnormal eye movements resembling oculogyric crisis [13]. Other observed symptoms include muscular hypotonia, self-injurious behaviours, and autism spectrum disorder [3].

The diversity of phenotypes observed across *GRIN1*-NDD patients has been attributed, in part, to the multitude of unique *GRIN1* gene variants. While variants are often unique to each patient, they tend to cluster near or within functionally important receptor domains, including the agonist-binding domains and transmembrane domain that forms the intrinsic ion channel pore of the NMDAR [1,2,13,14,15,16]. Individual variants have been found to enhance or diminish various properties of NMDARs and can be broadly classified as gain-of-function (GoF) or loss-of-function (LoF) [17]. While the location of certain gene variants has been linked to specific phenotypic features among *GRIN1*-NDD patients, including cortical malformation [3,14], such relationships remain ill-defined. Clinical differences are even inconsistent between patients possessing *GRIN1* variants categorized as NMDAR "GoF" or "LoF", posing a challenge to the development and delivery of *GRIN1*-NDD therapeutics. Therefore, in-depth study of individual variants is necessary to determine the unique functional consequences of variation on the NMDAR, to establish predictive variant-function relationships, and to ultimately guide patient treatment [18].

In this study we examine the p.Tyr647Ser (Y647S) variant which is located in the transmembrane domain M3 helix of GluN1 and is carried by a 33-year-old female with seizures and intellectual disability [2]. This variant falls within the highly conserved 646-654 residues of M3 known as the Lurcher (SYTANLAAF) motif. The motif is

thought to be crucial to the gating function of the receptor [13,19] and potentially to the trafficking of NMDARs to the cell surface [20]. *In vitro*, the Y647S variant reduces maximal glutamate-inducible current amplitudes in heterologous expression systems, and accompanying *in silico* models predict that the Y647S variant destabilizes quaternary structure of the transmembrane domain, disrupting NMDAR assembly [2]. The Y647S variant also reduces the surface delivery of NMDARs when expressed in HEK293 cells or in rat hippocampal neurons [21]. Together, these studies point to the Y647S variant as generating an NMDAR LoF phenotype [2, 17]. Nevertheless, Xu et al. (2024) classified the Y647S variant as one of indeterminant status [17], as NMDARs containing GluN1-Y647S display diminished open probability and surface expression (as noted in previous studies [21]) alongside increases in glutamate and glycine potency, compared to GluN1-WT containing NMDARs [22].

Here, we build upon the initial *in vitro* investigations by examining the molecular, electrophysiological, and behavioural consequences of the Y647S patient variant using a novel mouse model. Additionally, we aimed to validate the *Grin1*$^{Y647S/+}$ mouse as a representative model of key features of patient symptomology. Our comprehensive characterization reveals the Y647S variant confers a complex *in vivo* phenotype, which reflects largely diminished properties of NMDAR function. *Grin1*$^{Y647S/+}$ mice displayed neuroanatomical and behavioural abnormalities reminiscent of the individual carrying this variant and the broader clinical characteristics of *GRIN1*-NDD. Our findings underscore the utility of this model in future studies seeking to develop novel therapies and further understand the pathological mechanisms underlying NMDAR variation.

SUBJECTS/MATERIALS AND METHODS

MOLECULAR BIOLOGY AND TWO-ELECTRODE VOLTAGE CLAMP CURRENT RECORDINGS

The complementary DNA (cDNA) encoding the human GluN1-1a (referred to as GluN1; NM_007327.3) was utilized to generate the human *GRIN1*_p.Y647S variant by site-directed mutagenesis using the QuikChange protocol (Stratagene La Jolla, CA, USA) in the plasmid vector pCI neo as described previously [23]. Wild type (WT) or variant GluN1 subunit was co-expressed with human GluN2A (NM_000833.4) or human GluN2B (NM_000834.4) in pCI neo. The cDNA was linearized using DpnI (ThermoFisher, Waltham, MA) restriction digestion at 37°C for 1 hour. Complementary RNA (cRNA) was synthesized *in vitro* using the mMessage mMachine T7 kit (Ambion, Austin,

TX, USA) from linearized WT and variant cDNA (DpnI restriction digestion at 37°C for 1 hour; ThermoFisher, Waltham, MA).

Unfertilized *Xenopus laevis* stage VI oocytes were prepared from commercially available ovaries (Xenopus one Inc, Dexter, MI, USA) as described previously [24]. *Xenopus laevis* oocytes were injected with a 1:2 ratio of GluN1:GluN2A or GluN1:GluN2B cRNA and maintained in normal Barth's solution (in mM; 88 NaCl, 2.4 $NaHCO_3$, 1 KCl, 0.33 $Ca(NO_3)_2$, 0.41 $CaCl_2$, 0.82 $MgSO_4$, 10 HEPES, pH 7.4 with NaOH; supplemented with 100 µg/ml gentamycin, 40 µg/ml streptomycin) at 19°C for 2-3 days before recordings.

Two-electrode voltage clamp (TEVC) current recordings were performed at room temperature (23˚C) with the extracellular recording solution contained (in mM) 90 NaCl, 1 KCl, 10 HEPES, 0.5 $BaCl_2$, and 0.01 EDTA (pH 7.4 with NaOH) as previously described [23,25]. The voltage electrode and current electrode were filled with 0.3 M KCl and 3 M KCl, respectively. Current responses from oocytes were recorded under voltage clamp at holding potential (V_{HOLD}) -40 mV except for experiments that involved changes in the concentration of extracellular Mg^{2+} and Zn^{2+}, for which case V_{HOLD} was set at -60 mV and -20 mV, respectively. Glutamate concentration-response were recorded in the presence of saturating glycine, and glycine-concentration response curves were recorded in the presence of saturating glutamate. The concentration-response relationships for glutamate and glycine were fitted by *Equation 1*,

$$\textit{Response (\%)} = 100\% / (1 + (EC_{50} / [\ \textit{agonist}\ ])^{N}) \qquad \text{Eq. 1}$$

The concentration-response relationship for inhibition by Mg^{2+}, $Zn^{2+,}$ and H^{+} was recorded in the presence of saturating concentrations of both glutamate and glycine. Zn^{2+} concentration was buffered as previously described[17,26]. Concentration-response relationship for Mg^{2+}, Zn^{2+} and extracellular pH (proton concentration) were fitted by *Equation 2*,

$$\textit{Response (\%)} = (100\% - \textit{minimum}) / (1 + ([\ \textit{concentration}\ ] / IC_{50})^{N}) + \textit{minimum} \qquad \text{Eq. 2}$$

where EC_{50} is the concentration of the agonist (glutamate or glycine) that generates a half-maximal effect, IC_{50} is the concentration of the inhibitor/blocker that causes a half-maximal effect, *minimum* is the degree of residual response at a saturating concentration of the inhibitor/blocker, *N* is the Hill slope, and *Response* is indicated as a percentage of the fitted maximum.

The channel open probability (P_{OPEN}) was calculated from the degree *Potentiation* measured in MTSEA (2-aminoethyl methanethiol sulfonate hydrobromide, Toronto Research Chemicals, Ontario, Canada) using *Equation 3* [27]:

$$P_{OPEN} = (\gamma_{MTSEA} / \gamma_{CONTROL}) \times (1 / Potentiation) \qquad \text{Eq. 3}$$

where γ_{MTSEA} and $\gamma_{CONTROL}$ were the single channel chord conductance values estimated from GluN1/GluN2A receptors and fold *Potentiation* was defined as the ratio of current in the presence of MTSEA to current in the absence of MTSEA, and $\gamma_{MTSEA} / \gamma_{CONTROL}$ was 0.67 [27]. MTSEA solution was made fresh from powder stock and used within 30 minutes.

WHOLE CELL VOLTAGE CLAMP RECORDING AND BETA-LACTAMASE ASSAY

HEK293 cells (CRL 1573, ATCC, Manassas, VA, USA) were maintained in standard DMEM/Gluta-Max media (Thermo Fisher, Waltham, MA, USA) with 10% dialyzed fetal bovine serum (R&D Systems, Minneapolis, MN, USA) supplemented with 10 U/ml penicillin and 10 µg/ml streptomycin (Thermo Fisher, Waltham, MA, USA) at 37ºC and 5% CO_2. The calcium phosphate method was used to transiently transfect the cells with plasmid cDNA encoding green fluorescent protein (GFP) and NMDAR GluN subunits (5:1:1 for GFP:GluN1:GluN2A or variant GluN1-Y647S, 1:1:1 for GFP:GluN1:GluN2B or variant GluN1-Y647S), as previously described [28]. Whole cell voltage clamp (WCVC) recordings [23,28] were performed on the transfected HEK293 cells 24-48 hours post-transfection with external recording solution that contained (in mM) 150 NaCl, 10 HEPES, 30 D-mannitol, 3 KCl, 1 $CaCl_2$, and 0.01 EDTA (pH 7.4). The patch electrodes (resistance 3-5 MΩ) were prepared from thin-walled glass micropipettes (TW150F-4, World Precision Instruments, Sarasota, FL, USA) and filled with internal solution (in mM; 110 D-gluconate, 110 CsOH, 30 CsCl, 5 HEPES, 4 NaCl, 0.5 $CaCl_2$, 2 $MgCl_2$, 5 BAPTA, 2 NaATP and 0.3 NaGTP, pH 7.35). The current response was recorded (V_{HOLD}: -60 mV) using an Axopatch 200B amplifier (Molecular Devices, Union City, CA, USA) at room temperature (23ºC).

For the beta-lactamase surface expression assay, HEK293 cells were plated in 96-well plates (50,000 cells per well) and transiently transfected using Fugene6 (Promega, Madison, WI) with cDNA encoding a fusion protein of β-lac-WT GluN1 or β-lac-GluN1-Y647S and wild type GluN2B [29]. Eight wells were transfected with surface and total expression activities measured in 4 wells each 24 hr post-transfection. The absorbance at 486 nm was measured by a microplate reader at 30°C every min for 30 min. The ratio of surface (unlysed cells) to total (lysed cells) beta-lactamase

expression was measured for the blac-GluN1-Y647S and compared to blac-GluN1-WT as described previously [29]. All chemicals were purchased from Sigma-Aldrich unless otherwise stated.

MICE AND GENOTYPING

Mice were housed with littermates on a 12-hour light-dark cycle with food and water available *ad libidum*. All experimentation was conducted during the light phase. Animal housing and experiments were conducted in accordance with the Canadian Council on Animal Care and the University of Toronto Faculty of Medicine and Pharmacy Animal Care Committee.

Grin1$^{Y647S/+}$ (Y647S/+) mice were created via CRISPR-Cas9 endonuclease-mediated transgenesis. Founder mice were identified by Sanger sequencing and bred to a C57BL/6J background to generate Wildtype (WT, +/+) and Y647S/+ mice. Mice were genotyped using two separate PCRs for each allele: the WT and Y647S variant allele (which is a two base pair difference). Therefore, each PCR reaction is completed with either the WT primers or Y647S variant allele amplification primers (339-bp amplicon) (along with a control reaction for PCR); WT - forward: GAT CAT CGT GGC TTC CTA reverse: CTC AGC TGC ACT CTC ATA AT ; Y647S - forward: GAT CAT CGT GGC TTC TTC reverse: CTC AGC TGC ACT CTC ATA AT. Touchdown PCR was used with DreamTaq DNA Polymerase (Thermo Fisher Scientific): 2 min at 96 degrees, then each cycle after is 94 degrees for 20 seconds, annealing for 30 seconds. The initial 12 cycles are touchdown from 64-58 degrees (0.5 degrees/cycle), with the remaining 28 cycles with an annealing temperature of 58 degrees (40 cycles total), with extension of 30 seconds for each cycle.

RNA ISOLATION AND RT-QPCR

Mice were euthanized by cervical dislocation and RNA from forebrain was extracted using TRIzol Reagent (Thermo Fisher Scientific). cDNA was synthesized using an Invitrogen Superscript III Reverse Transcriptase kit (Thermo Fisher Scientific) using 1 μg of sample. Quantitative RT-qPCR was performed on a QuantStudio 5 (Applied Biosystems). Melt curve analysis was used to check reaction specificity. All data was normalized to PGK1-2. Primers were as follows: *Grin1*- forward: ACA CCA ACA TCT GGA AGA CAG reverse: CAG TCA CTC CAT CTG CAT ACT T, *Grin2a* – forward: ACC ATT GGG AGC GGG TAC AT reverse: CCT GCC ATG TTG TCG ATG TC, *Grin2b* – forward: TCC GCC GTG AGT CTT CTG reverse: CTG GGT GGT AAA GGG TGG, *PGK1-2* – forward: GGC CTT TCG ACC TCA CGG reverse: GTC CAC CCT CAT CAC GAC.

WESTERN BLOT PROTEIN ANALYSIS

Mice were euthanized by cervical dislocation and total brain protein lysates were prepared by homogenizing right brain hemispheres in 0.32 M HEPES -buffered sucrose and a protease inhibitor cocktail (PMSF, aprotinin, leupeptin, pepstatin and benzamidine). Synaptic plasma membrane fractions were obtained using a discontinuous sucrose gradient as described previously [30]. Protein concentration of samples was determined using Bradford protein assay using bovine serum albumin standards. Protein samples (10 μg/lane) were separated on a 10% Tris-glycine gel (Thermo Fisher Scientific) and transferred to a PVDF membrane (Millipore). Blocking of non-specific binding was completed in 3% milk in Tween-Tris buffered saline (TBST) for 1 hour. Primary antibodies were diluted in 3% milk in TBST and incubated overnight at 4 degrees. Antibodies used: NMDAR1 (1:1000; Millipore, Cat# AB9864R), NMDAR2A (1:1000, Millipore, Cat# AB1555P), NMDAR2B (1:1000; Millipore, Cat# AB1557P). Secondary goat anti-rabbit antibody (LI-COR Biosciences; Cat# 926-32213) was diluted at 1:5000 in 3% milk in TBST. Blots were normalized to Revert 700 Total protein stain, visualized using the Odyssey M Imager, and relative band intensities were quantified using Empiria Studio Software (LI-COR Biosciences).

HIPPOCAMPAL SLICE ELECTROPHYSIOLOGY

Hippocampal slices were prepared from adult (12–15 week) male and female Y647S/+ mice and their wildtype (+/+) littermate counterparts. Mice were euthanized by cervical dislocation under isoflurane anaesthesia and brains were rapidly extracted and submerged in ice-cold cutting solution composed of (in mM): 205 Sucrose, 26 $NaHCO_3$, 10 Glucose, 2.5 KCl, 1.25 NaH_2PO_4, 0.5 $CaCl_2$, and 5 $MgSO_4$ (saturated with 95% O_2 and 5% CO_2; pH 7.4). After being allowed to cool for 2 – 3 min, brains were hemisected along the longitudinal fissure and slices of dorsal hippocampus (400 μm) were obtained by sectioning each hemisphere along its sagittal plane using a VT1200S vibratome (Leica). The CA3 region of slices was removed by scalpel cut immediately after slicing. Slices were then allowed to recover for a minimum of 1 h at room temperature in standard artificial cerebrospinal fluid (ACSF) composed of (in mM): 124 NaCl, 26 $NaHCO_3$, 10 Glucose, 3 KCl, 1.4 NaH_2PO_4, 2 $CaCl_2$, and 1 $MgSO_4$ (saturated with 95% O_2 and 5% CO_2; pH 7.4).

Following recovery, slices were transferred to a submerged-type chamber where they were continuously perfused with ACSF (2.5 mL/min) and maintained at 30 °C for extracellular field potential recordings which were performed blind to genotype. Glass microelectrodes (~1.5 MΩ) filled with ACSF were used to record fibre volleys (FVs) and field excitatory postsynaptic potentials (fEPSPs) from CA1 stratum radiatum in response to stimulation of

the Schaffer collateral/commissural (SC) pathway. Constant current stimulus pulses (100 µs) were generated by an STG4002 stimulus isolator (Multi Channel Systems) and delivered via a platinum/iridium bipolar stimulating electrode (FHC) positioned in the stratum radiatum near the CA1/CA2 border. Signals were amplified using a Multiclamp 700B (Molecular Devices), filtered at 2 kHz, digitized at 40 kHz, and recorded to a personal computer for offline analysis using WinLTP software [31].

For each slice, stimulus intensity was determined as a function of the threshold required to elicit a visually detectable response. Input/output (I/O) curves were generated by delivering stimuli at multiples of this threshold value (1– 5×). Baseline stimulus intensity for paired-pulse facilitation (PPF) and long-term potentiation (LTP) experiments was set to 3× the threshold value to evoke sub-maximal AMPAR-mediated fEPSPs (AMPAR-fEPSPs). Test pulses were delivered every 30 s, and four consecutive responses were averaged for analysis. PPF was assessed across a range of inter-pulse intervals (50, 100, 150, 200 and 250 ms). NMDAR-mediated fEPSPs (NMDAR-fEPSPs) were recorded in low (0.1 mM) magnesium ACSF in the presence of the AMPAR blocker NBQX (10 µM). For plasticity experiments, LTP was induced after 30 min of stable baseline recording by delivering a theta-burst stimulation (TBS) protocol comprising 3 episodes of 5 bursts of 5 pulses at 100 Hz repeated at 5 Hz, with a 10 s interval between each episode. FVs were quantified by their peak amplitudes and fEPSPs were quantified by their initial slopes. I/O curves from individual slices were quantified by plotting the FV amplitude as a function of stimulus intensity or the fEPSP slope as a function of FV amplitude and taking the slope value of the fitted linear regression line (I/O slope).

HISTOLOGY

Adult male and female mice (13-21 weeks) were euthanized by cervical dislocation and brains were fixed in 10% neutral buffered formalin (Fisher Scientific) for 48 hours. Brains were subsequently dehydrated in 70% ethanol, processed, and embedded into paraffin. Sections were cut sagittally 1.525 mm lateral of Bregma at 5 µm thickness and stained with hematoxylin and eosin or Nissl stain. Brain sections were imaged using the Axioscan 7 Slide Scanner (Zeiss) and subsequently analyzed using QuPath v0.3.2 [32] blind to genotype. The number of cortical neurons was counted in a 1.44 mm^2 region and thickness measurements were completed using line annotations of the neocortex and hippocampus (including individual measurements of CA1, CA2 and dentate gyrus regions), in a manner similar to Amador et al. (2020) [33]. Contour tracing for cell body area measurements of the hippocampus proper and dentate

gyrus was applied using the QuPath wand tool and fine-tuned using the brush tool in a manner similar to Edwards et al. (2020) [34].

EARLY DEVELOPMENTAL BEHAVIOURAL PHENOTYPING

ULTRASONIC VOCALIZATIONS (USVs)

USVs were collected at postnatal day (P) 6 in mice of both sexes. Pups were taken in random order from their home cages (containing littermates and mother), and each placed individually into a clean empty cage within a transparent sound attenuating chamber (33.5 x 21.5 x 30.5 cm). The three-minute trial began immediately after the pup was placed into the chamber and lid had been closed. USV recordings were captured using an Avisoft UltraSoundGate condenser microphone CM16 (Avisoft Bioacoustics, Berlin, Germany), sensitive to 10-180 kHz. The microphone was mounted on a clamp located within the sound attenuating chamber approximately 19 cm away from the pup being recorded. Vocalizations were recorded using Avisoft Recorder Software at 250 kHz sampling rate and 16-bit resolution. Analysis was completed using DeepSqueak software v3.1.0 [35] by an experimenter blinded to genotype. This was done using the Mouse Detector YOLO R2 Neural network with 30 kHz lower frequency and 110 kHz upper frequency cutoffs [36, 37], with a total analysis length of 180 seconds. Score threshold was set to 0, meaning all detections were saved to the file. Calls were visualized using the “Load call” function, and a manual selection review was conducted by an experienced experimenter.

Following collection of USVs, the righting reflex was tested by placing the pup on its back in a clean cage and recording the time it takes for the pup to return to the prone position with all paws placed on the ground. The maximum trial length allotted was one minute.

WIRE HANG

Wire hang was performed to assess motor function and muscle strength in P21 male and female mice. A wire cage hopper was placed across an empty cage. Each mouse was allowed to grasp the wire cage hopper that was then carefully inverted over the empty cage. Once inverted, the latency to fall was recorded with a maximum allotted trial length of three minutes. Body weight was collected after the completion of the trial. Holding impulse was calculated as latency to fall (s) x bodyweight (kg) [38,39].

ADULT BEHAVIOURAL PHENOTYPING

All adult neurobehavioral tests were done in male and female mice between 12-22 weeks of age (except for behavioural convulsion tracking) and conducted in the daytime when the lights were on between 7 am and 7 pm. In most cases, mice were experimentally naive at the time of behavioural testing and were not handled by experimenters prior to testing (outside of standard animal husbandry).

WIRE HANG

Wire hang was performed in adult mice to re-assess motor function and muscle strength. A wire cage hopper was placed across an empty cage, held up by two cages on either side. Each mouse was allowed to grasp the wire cage hopper which was then subsequently inverted over the empty cage. Once inverted, the latency to fall was recorded with a maximum allotted trial length of one minute. This was immediately repeated twice more, for a total of three one-minute trials. Body weight was collected after the completion of all trials. Latency to fall was averaged across the three trials and holding impulse was calculated as average latency to fall (s) x bodyweight (kg) [38,39].

OPEN FIELD TEST

Mice were placed individually into a transparent plexiglass chamber (20 x 20 x 45 cm) for 2 hours, during which locomotor and stereotypic behaviour were recorded using digital activity monitors (Omnitech Electronics, Columbus, OH, USA). Individual square chambers were quadrants within a larger area subdivided by a transparent plexiglass "+" insert. The majority of mice were tested with a sex-matched partner in the diagonally adjacent chamber, but in some cases, mice were tested individually if no compatible companion was available. Infrared light beam sensors were used to track the animal's total distance traveled and the number of stereotypic movements within 5-minute bins.

BEHAVIOURAL CONVULSION TRACKING

Starting at ages 7-19 weeks, mice were monitored once weekly for 12 weeks for the presence of behavioural convulsions. During monitoring, mice were handled for one minute in a biological safety cabinet and subsequently weighed. The presence or absence of a behavioural convulsion was recorded for each mouse and if present was captured on video. If a behavioural convulsion was elicited, the mouse was allowed to recover before weighing and being returned to the home cage.

Behavioural convulsion severity was rated from videos using the categories depicted in Table S1. Convulsion categories were additive, for example, the most severe convulsions included bouts of jumping and backing up in addition to characteristics seen in preceding categories.

AUDIOGENIC SEIZURE TESTING

Audiogenic seizure testing was conducted as described in Wong et al. (2023) [40]. The testing apparatus consisted of a soundproof box containing a plastic mouse cage (28 x 17 x 14 cm) outfitted with a sound source (125 dB Piezo siren, electrosonic; Piezo Technologies) on the lid, which extended 5 cm into the cage. Mice aged 21-22 weeks (males n = 8 +/+, n = 4 Y647S/+, females n = 5 +/+, n = 10 Y647S/+) were individually placed in the cage within the test apparatus and allowed to explore for a 2-min habituation period. Immediately thereafter, the sound source was played for 3 min. Video was recorded throughout the habituation and audiogenic siren sessions, and seizure activity was scored using a standard 4-point severity scale, as in Wong et al. (2023) [40].

SOCIAL INTERACTION TEST

Sociability was tested using a procedure adapted from the three-chamber apparatus [41], in which there were no dividing walls (resulting in a singular unobstructed arena). Mice were placed in an opaque-white walled plexiglass arena (62 x 40.5 x 23 cm). The arena contained two identical inverted wire cups: one empty (non-social, NS) and one containing a novel age and sex-matched WT mouse of the same genetic background (social, S). The location of the social cup in the left vs. right side of the arena was systematically alternated between trials. Over a 10-min period, the test mouse was video recorded, and its movements were automatically tracked and analyzed using Biobserve Viewer2 software (St. Augustin, Germany). Around each inverted wire cup, a circular zone with a radius of 5 cm was defined. Sociability was measured as the time spent in the 5-cm social zone around the cup containing the novel mouse versus the time spent in the 5-cm non-social zone around the empty cup. Mice that climbed on top of either the non-social or social cup during the trial were excluded from the analysis.

ELEVATED PLUS MAZE

The elevated plus maze is a well-validated assay of anxiety-like behaviour in mice. In this study, the location of the mouse was tracked continuously within two “open” (25 x 5 cm) and two enclosed arms (25 x 5 x 30 cm) of an elevated arena (50 cm). The two arms of each type were arranged across from one another, extending from a central area (5 x 5 cm) in a ‘+’ configuration. Trials were conducted in dim light with light of ~75 lux illuminating the open arms. Each mouse was placed in the central area of the elevated plus maze facing an open arm and allowed to explore the

maze for 8 minutes. Each mouse was video-recorded and its movements were tracked and analyzed using Biobserve Viewer2 software (St. Augustin, Germany). The number of entries and time spent in each type of arm and the center was measured, as well as the total distance travelled in the maze. Subsequently, the percentage of time spent in the open arms was calculated by dividing the total time spent in the open arms by the total length of the test (480 seconds) and multiplying by 100.

PUZZLE BOX

The puzzle box procedure was adapted from Ben Abdallah et al. (2011) and was used to assess executive function and cognitive flexibility [42]. The puzzle box arena consisted of a white opaque plexiglass box divided by a removable barrier, creating two compartments: a bright starting zone (58 cm x 28 cm) and a goal zone covered by a retractable roof (15 cm x 28 cm) that contained a mouse shelter (Lantz Enterprises Inc., Hamilton, Canada). An underpass (4 cm wide) was located beneath the barrier connecting the starting and goal zones. The experimental protocol consisted of seven trials (T1-7) over three consecutive days, with three trials per day (except for the third day). Across the trials, mice were presented with increasingly difficult obstacles constraining their path through the underpass into the goal zone. On day 1 T1, which was considered the training trial, the underpass was open and the barrier had an open door located above the underpass (4 cm x 4 cm). On T2 and T3, the doorway in the barrier was removed and the mice had to enter the goal zone exclusively via the underpass. On day 2, T4 was identical to T2 and T3, where mice must again enter the goal zone through the underpass. On T5-T6 (day 2) and T7 (day 3) the underpass was filled with clean bedding, which the mice had to dig through in order to reach the goal zone. This trial sequence allows for the testing of cognitive flexibility and problem solving through exposure to novel tasks (T2 and T5), including short- and long-term memory through repetition of specific obstacles 2 min (T3 and T6) and 24h (T4 and T7) after the initial exposure, respectively. Trials were started by placing the mouse at the end of the start zone furthest from the barrier/underpass and ended when the mouse entered the goal zone with all four paws. Upon entry to the goal box, mice were allowed to remain for 1 min. Mice were then removed and placed in a clean cage for 1 min before beginning the next trial. Mouse performance was assessed using latency to enter the goal box on each trial, with a maximum of 5 min allotted to each trial.

STATISTICAL ANALYSIS

Data are presented as the mean ± SEM and error bars represent SEM unless otherwise stated. Statistical analyses were performed in GraphPad Prism v. 10.1.1 (GraphPad Software, San Diego, CA) and OriginPro 9.0

(Northampton, MA, USA), using unpaired t-tests or 2-way analysis of variance (ANOVA), followed by Tukey's multiple comparisons post-hoc test when appropriate. Power was determined using GPower (3.1.9.2). Data from male and female mice were combined for statistical analyses, except for analyses performed for P6 USVs, adult bodyweight, and holding impulse. In these instances, males and females are represented in circle and triangle symbols respectively. For hippocampal electrophysiology, two slices per animal from six animals were used in each experimental group. Statistics were performed using the number of slices. Simple linear regression was used to estimate the relationship between seizure frequency and severity as a function of weeks of monitoring.

RESULTS

NMDARs containing GluN1-Y647S have altered sensitivity to agonists and negative modulators in oocytes

To investigate the effects of GluN1-Y647S variant subunits on NMDAR function *in vitro*, GluN1-Y647S-containing variant NMDARs or WT GluN1 were co-expressed with either WT GluN2A or GluN2B subunits in *Xenopus laevis* oocytes. Currents from oocytes expressing recombinant NMDARs were recorded under voltage clamp at -40 mV in response to the application of endogenous agonists. Concentration-response curves were generated for the NMDAR co-agonists glutamate and glycine to determine EC_{50} values and assess the potential effects of the GluN1-Y647S variant on agonist potency. For L-glutamate concentration-response studies, GluN1-Y647S-containing NMDARs displayed significantly (non-overlapping of 95% confidence intervals determined from $LogEC_{50}$) reduced L-glutamate EC_{50} values (reflecting enhanced potency) compared to WT GluN1 when co-expressed with GluN2A (GluN1-Y647S EC_{50}: 0.074 μM; WT GluN1 EC_{50}: 3.2 μM) **(Figure 1B; Table 1)** or GluN2B (GluN1-Y647S EC_{50}: <0.01 μM; WT GluN1 EC_{50}: 1.5 μM) (**Figure S1A; Table 1**). Similar results were found for the glycine EC_{50} of GluN1-Y647S-containing NMDARs, which was significantly reduced compared to WT GluN1 when co-expressed with GluN2A (GluN1-Y647S EC_{50}: 0.036 μM; WT GluN1 EC_{50}: 1.2 μM) **(Figure 1B; Table 1)** and GluN2B (GluN1-Y647S EC_{50}: 0.017 μM; WT GluN1 EC_{50}: 0.41 μM) **(Figure S1B; Table 1)**. Therefore, the GluN1-Y647S variant enhances agonist potency of L-glutamate and glycine as indicated by significant reductions in EC_{50} values.

Concentration-response curves were also generated for endogenous negative allosteric modulators of the NMDAR, including extracellular Mg^{2+}, Zn^{2+}, and protons, to determine IC_{50} values and to assess the potential effects of the GluN1-Y647S variant on sensitivity to inhibition. The Mg^{2+} concentration-response relationship was recorded at -60 mV, which revealed that the Mg^{2+} IC_{50} was significantly reduced in GluN1-Y647S-containing NMDARs

compared to NMDARs that contained WT GluN1 co-expressed with GluN2A (GluN1-Y647S IC_{50}: 12 μM; WT GluN1 IC_{50}: 22 μM (**Figure 1C; Table 1**). The Mg^{2+} IC_{50} value for GluN1-Y647S (IC_{50} 15 μM) was comparable to WT GluN1 (IC_{50} 22 μM) when co-expressed with GluN2B (**Figure S1C; Table 1**). When co-expressed with GluN2A, the NMDARs containing the GluN1-Y647S variant did not display significant changes to the IC_{50} of Zn^{2+} (GluN1-Y647S IC_{50} 9.9 nM; WT GluN1 IC_{50} 7.9 nM) compared to NMDARs expressing WT GluN1 **(Figure 1D; Table 1**). However, the maximal degree of voltage-dependent inhibition examined in the presence of 300 nM Zn^{2+} was significantly decreased for GluN1-Y647S (47 ± 4.4 %) compared to WT GluN1 (61 ± 3.3 %) (**Table 1**). In addition, the influence of the Y647S variant on extracellular proton (H^+) sensitivity was evaluated by comparing the ratio of current response recorded at pH 6.8 to pH 7.6 at a holding potential of -40 mV. When co-expressed with GluN2A, GluN1-Y647S-containing NMDARs displayed significantly enhanced inhibition at pH 6.8 (GluN1-Y647S 26 ± 0.66%; WT GluN1 42 ± 0.74%) (**Figure 1E, Table 1**), consistent to the concentration-response curves, which showed that the variant NMDARs have an IC_{50} value corresponding to pH 7.0 ($1.01x10^{-7}$ M), compared with pH 7.2 ($6.55x10^{-8}$ M) for WT GluN1 co-expressed with WT GluN2A **(Figure 1E, Table 1)**. However, when expressed with WT GluN2B, GluN1-Y647S had significantly reduced proton inhibition (GluN1-Y647S 21 ± 0.99 %; WT GluN1 15 ± 0.70 %) (**Figure S1D, Table 1**). Therefore, the GluN1-Y647S variant displayed increased sensitivity to Mg^{2+} channel block and decreased sensitivity to maximal inhibition by Zn^{2+}. The GluN1-Y647S variant showed altered levels of proton inhibition, which could change tonic levels of proton inhibition at physiological pH. Variant GluN1 showed enhanced inhibition when co-expressed with GluN2A and reduced when co-expressed with GluN2B.

NMDARs containing GluN1-Y647S affect channel biophysics and cell surface trafficking in HEK cells

To determine if the GluN1-Y647S variant alters the agonist-induced current response time course, whole cell current responses were recorded under voltage clamp at -60 mV from transiently transfected HEK cells with WT GluN1 or GluN1-Y647S co-expressed with either GluN2A or GluN2B. In response to rapid agonist application for brief duration (5 ms) and rapid removal of 1 mM glutamate in the presence of 100 μM glycine to mimic synaptic events, the current amplitude of HEK cells co-expressing GluN1-Y647S with WT GluN2A was significantly reduced compared to those expressing WT GluN1 with WT GluN2A (GluN1-Y647S 0.29 ± 0.08 pA/pF; WT GluN1 138 ± 31 pA/pF) (**Figure 1F, G; Table 1**) and GluN2B (GluN1-Y647S 0.06 ± 0.03 pA/pF; WT GluN1 49 ± 11 pA/pF) (**Figure**

S1E, Table 1). The amplitude of the whole cell current response mediated by NMDARs depends on several factors, including the channel open probability and receptor surface expression [17]. Thus, these properties were evaluated to better understand the substantial (>100-fold) reduction in current response amplitude observed in HEKs transiently transfected with GluN1-Y647S-containing GluN1. Channel open probability of the variant was assessed by the degree of MTSEA potentiation by TEVC oocyte recordings at a holding potential of -40 mV. When co-expressed with GluN2A, NMDARs containing the GluN1-Y647S variant displayed a significant decrease in open probability (GluN1-Y647S calculated P_{OPEN} 0.048 ± 0.005; WT GluN1 calculated P_{OPEN} 0.28 ± 0.02) (**Figure 1H, Table 1**). To evaluate whether the GluN1-Y647S variant alters receptor surface expression, a beta-lactamase (β-lac) assay was utilized to measure cell surface and total protein levels. In the assay, β-lac was fused in frame to the extracellular aminoterminal domain of WT GluN1 (β-lac-GluN1-Wt) and the variant GluN1-Y647S (β-lac-GluN1-Y647S). The β-lac-GluN1 fusion protein was co-expressed with GluN2B in HEK cells and the level of surface receptor expression was determined by β-lac cleavage of the cell-impermeable chromogenic substrate nitrocefin in the extracellular solution [29, 43]. When co-expressed with GluN2B, the GluN1-Y647S variant containing receptor displayed a 0.44 ± 0.11 surface/total ratio, relative to the 1.0 surface/total ratio assigned to WT GluN1, representing a significant reduction in NMDARs reaching the surface of the cell **(Figure S1F, Table 1)**. Xu et al. (2024) likewise found a markedly lower surface/total ratio in GluN1-Y647S variant containing receptors compared to WT GluN1 when co-expressed with GluN2A (**Table 1, data shown for comparison**) [22]. Therefore, the GluN1-Y647S variant appears to diminish NMDAR channel open probability and surface expression, contributing to the overall reduction in whole cell current response.

Generation and molecular characterization of *Grin1*$^{Y647S/+}$ variant mice

To examine the consequences of the *Grin1*-Y647S (Y647S/+) variant *in vivo*, a mouse model harboring the orthologous point mutation was generated using CRISPR-Cas9 endonuclease-mediated transgenesis on a C57BL/6J genetic background **(Figure 2A,B)**. *Grin1*$^{Y647S/+}$ variant offspring were generated in expected Mendelian ratios and showed normal survival and postnatal weight gain and growth from P6-10 **(Data not shown)**.

Abundance of *Grin1* as well as *Grin2a* and *2b* mRNA in the forebrain of adult WT and *Grin1*$^{Y647S/+}$ brain were not statistically different, indicating that the Y647S/+ mouse variant had no effect on gene transcripts for these NMDAR subunit components **(Figure 2C)**. Western blot protein analysis of whole brain from adult *Grin1*$^{Y647S/+}$

indicated that GluN1 protein levels were modestly but significantly lower ($p = 0.0361$), whereas GluN2A and GluN2B levels were unaffected **(Figure 2D,E)**. However, GluN1, 2A, and 2B protein expression in purified synaptic membrane of *Grin1*$^{Y647S/+}$ mice were equivalent to WT **(Figure 2D, F)**. These results suggest that apart from a reduction in whole brain GluN1 level, the heterozygous Y647S variant has minimal impact on abundance of GluN1, 2A, and 2B protein and their corresponding mRNAs.

Deficiency in hippocampal NMDAR-mediated synaptic transmission and long-term potentiation

NMDARs contribute to cellular excitability and regulate synaptic strength; hence we used *ex vivo* hippocampal CA1 field potential recordings in hippocampal slices to identify differences in synaptic transmission and long-term potentiation for adult WT versus *Grin1*$^{Y647S/+}$mice **(Figure 3A)**. Fibre volley (FV) amplitude was measured in response to step wise increases in stimulus current intensity. The corresponding slopes of the I/O curves for FV vs. stimulus intensity did not significantly differ between WT and *Grin1*$^{Y647S/+}$ mice, demonstrating largely unaffected presynaptic axon activation in *Grin1*$^{Y647S/+}$ mice **(Figure 3B)**. Similarly, paired-pulse facilitation, which is inversely related to neurotransmitter release probability, did not differ significantly between WT and *Grin1*$^{Y647S/+}$ mice **(Figure 3D)**. Together these results suggest that no major alterations in presynaptic function are caused by the *Grin1*-Y647S variant in the hippocampal CA3-CA1 Schaffer-collateral pathway.

Furthermore, the *Grin1*-Y647S variant had no effect on AMPAR-mediated synaptic transmission as measured by the slope of the I/O curve plotting AMPAR-fEPSP slope as a function of FV amplitude **(Figure 3C)**. In contrast, recordings performed in the presence of low magnesium and the AMPAR blocker NBQX revealed significantly reduced NMDAR-fEPSP slope as function of FV amplitude ($p < 0.0001$), indicating the *Grin1*-Y647S variant caused a near-complete absence of hippocampal NMDAR-mediated synaptic transmission **(Figure 3E)**. To assess the impact of the *Grin1*-Y647S variant on synaptic plasticity, long-term potentiation at CA3-CA1 synapses was induced using a compressed TBS protocol. The magnitude of LTP (average fEPSP slope change 80-90 min post TBS) was significantly reduced in *Grin1*$^{Y647S/+}$ mice ($p < 0.0001$), indicating substantial impairment in synaptic plasticity mechanisms **(Figure 3F)**.

Adult *Grin1*$^{Y647S/+}$ variant mice have altered hippocampal morphology

A subset of individuals with *GRIN1*-NDD display malformations of cortical development [3], therefore the potential for gross histological changes were evaluated in the neocortex, in addition to the hippocampal subfields including the dentate gyrus. Neocortical features including thickness **(Figure 4C)** and density of neurons **(Figure 4D)** were found to be unaltered in adult *Grin1*$^{Y647S/+}$ mice. In contrast, the area of the hippocampal pyramidal cell layer was found to be smaller in *Grin1*$^{Y647S/+}$ mice ($p = 0.0290$) (**Figure 4F)**. Cell body area and the thickness of the dentate gyrus, as well as thickness of the CA1 and CA2 hippocampal subfields, were found to be unaltered (**Figure 4F, G**).

Alterations in communication and muscle strength in *Grin1*$^{Y647S/+}$ postnatal development

Given the profound alterations to NMDAR function associated with the *Grin1*$^{Y647S/+}$variant, cognitive and behavioural manifestations are anticipated in the heterozygous mouse model. For instance, *GRIN1*-NDD in general is characterized by mild-to-profound developmental delay that includes muscular hypotonia (66% of patients) and absent speech in 48% of individuals [3]. Thus, communicative and motor capabilities of *Grin1*$^{Y647S/+}$ variant mice were evaluated. At P6, the righting reflex of *Grin1*$^{Y647S/+}$ variant mice (34 ± 4.6 seconds) was present and did not significantly differ from WT (25 ± 3.6 seconds), indicating typical trunk motor control **(Figure 5A).** However, in response to maternal isolation, P6 *Grin1*$^{Y647S/+}$ variant pups displayed significantly more ultrasonic vocalizations in comparison to WT counterparts (two-way ANOVA main effect of genotype: $F[1,64] = 8.891$; $p = 0.0046$). There was a modest interaction between the effects of genotype and sex (two-way ANOVA genotype x sex interaction: $F[1,64] = 3.613$, $p = 0.0618$), as P6 *Grin1*$^{Y647S/+}$ male pups appeared to display more vocalizations in comparison to WT counterparts, while female *Grin1*$^{Y647S/+}$ did not. This may be driven by an apparent increased number of ultrasonic vocalizations in female WT compared to male WT pups **(Figure 5B)**. At P21, *Grin1*$^{Y647S/+}$ mice (7.6 ± 0.21 grams) displayed significantly reduced bodyweight compared to WT (8.2 ± 0.21) ($p = 0.0383$), in addition to deficits in muscle tone indicated by significantly reduced holding impulse in the wire hang task ($p = 0.0120$) **(Figure 5C, D**).

Adult *Grin1*$^{Y647S/+}$ variant mice display hyperactivity and spontaneous convulsions

In adulthood, there was a statistically significant interaction between the effects of genotype and sex on the bodyweight of mice (two-way ANOVA genotype × sex interaction: $F[1,83] = 9.430$, $p =0.0029$), with significant reductions in *Grin1*$^{Y647S/+}$ variant bodyweight maintained in both males (WT 28 ± 0.85 grams; *Grin1*$^{Y647S/+}$ 24 ± 0.53

grams; Tukey's post hoc test: $p < 0.0001$) and females (WT 23 ± 0.29 grams; *Grin1*$^{Y647S/+}$ 19 ± 0.37 grams; Tukey's post hoc test: $p = 0.0137$) **(Figure 6A)**. However, holding impulse in the wire hang task did not differ, indicating recovery of muscle tone deficits seen in *Grin1*$^{Y647S/+}$ mice at P21 **(Figure 6B)**.

In the open field test, *Grin1*$^{Y647S/+}$ variant mice traveled a significantly greater distance over the 2-hour trial compared to WT mice ($p = 0.001$) **(Figure 6C)**. There was a statistically significant interaction between the effects of genotype and time on distance traveled in the open field test (two-way ANOVA genotype x time interaction: $F[23,989] = 16.65$, $p < 0.0001$), with *Grin1*$^{Y647S/+}$ variant mice traveling significantly greater distance within each of the 5-min bins between time = 0 – 25 and 35 min (Tukey's post hoc tests: 5, $p < 0.0001$; 10, $p = 0.0013$; 15, $p = 0.0014$; 20, $p = 0.0012$; 25, $p = 0.0460$; 35, $p = 0.0281$), but not thereafter, indicating initial hyperlocomotion but intact habituation to the novel open field environment **(Figure 6D)**. The number of stereotypic or repetitive movements exhibited during the open field test did not differ between genotypes **(Figure 6E)**.

A prominent clinical symptom of *GRIN1*-NDD that also afflicts the individual carrying the Y647S/+ variant is the presence of seizures. During weekly handling by experimenters for a duration of 12 weeks, spontaneous convulsions were completely absent in WT mice, but became increasingly evident in *Grin1*$^{Y647S/+}$ variant mice, with 71% (10/14 mice) displaying convulsion in the final week of monitoring (aged 19 – 30 weeks) **(Figure 6F)**. Simple linear regression was used to test if the number of weeks of monitoring predicted the frequency of convulsions observed in the group of Y647S/+ mice. The fitted regression model was: number of convulsions observed in a week = 0.8462* (weeks of monitoring) - 1.167. The overall regression was statistically significant ($r^2 = 0.8628$, $F(1,10) = 62.88$, $p < 0.001$). Thus, the cumulative number of weekly monitoring sessions significantly predicted the number of convulsions observed in the group of Y647S/+ mice **(Data not shown)**. Convulsion severity was evaluated using the scale described in **Table S1, Figure 6G,** and depicted as a heat map in **Figure 6H**. Simple linear regression was used to test if the cumulative number of weekly monitoring sessions predicted the average severity of convulsions observed in the group of Y647S/+ mice. The fitted regression was: average severity of convulsion = 0.2225*(weeks of monitoring) - 0.4048. The overall regression was statistically significant ($r^2 = 0.8813$, $F(1,10) = 74.21$, $p < 0.001$). Thus, the cumulative number of weekly monitoring sessions also predicted the average severity of convulsion observed in the group of Y647S/+ mice **(Data not shown)**.

Grin1$^{Y647S/+}$ variant mice are not susceptible to audiogenic convulsions

When exposed to a 125 dB audiogenic sound stimulus, WT and *Grin1*$^{Y647S/+}$ variant mice did not display susceptibility to convulsions. Only one (of a total of 14 *Grin1*$^{Y647S/+}$ variant mice tested) displayed wild running, which was assigned the lowest severity score of 1 and hence was not categorized as a seizure [40] **(Data not shown)**.

Alterations in problem solving, sociability, and anxiety-like behaviours in adult *Grin1*$^{Y647S/+}$ variant mice

The social interaction test evaluates the predilection of mice to interact with a caged, same-sex stranger mouse rather than an empty cage. In this test there was a statistically significant interaction between the effects of genotype and the type of stimulus (social or non-social) (two-way ANOVA genotype x stimulus interaction: $F[1,46] = 13.36$, $p = 0.0007$). Both genotypes spent significantly more time with the social stimulus than the non-social (Tukey's post hoc test: +/+ $p = 0.0159$; Y647S/+ $p < 0.0001$) **(Figure 7A)**. Interestingly, *Grin1*$^{Y647S/+}$ variant mice also spent significantly less time with the non-social stimulus compared to WT (Tukey's post hoc test: $p = 0.0169$), which may indicate exaggerated sociability **(Figure 7A)**.

Anxiety-like behaviour can be modeled using the elevated plus maze, measured as the percentage of time spent in the open arms over the course of the session. *Grin1*$^{Y647S/+}$ variant mice spent a significantly greater percentage of time in the open arms compared to WT mice ($p < 0.0001$), interpreted as a reduction in anxiety-like behaviour **(Figure 7B)**.

Finally, *Grin1*$^{Y647S/+}$ mice were tested in the puzzle box task. In this test mice travel from a brightly lit arena to a darkened goalbox through increasingly challenging impediments to assess executive function and cognitive flexibility. There was a statistically significant interaction between the effects of genotype and trial on the latency to reach the goal box (two-way ANOVA genotype x trial interaction: $F[6, 138] = 4.310$, $p = 0.005$). Comparable latencies were exhibited by *Grin1*$^{Y647S/+}$ and WT mice during Trial 1 (T1), suggesting normal preference of each group to enter the goalbox via an open door **(Figure 7C)**. Likewise, latencies were comparable between the genotypes during T2, the first trial in which mice must traverse an underpass to reach the goal box. However, upon first exposure to a bedding-filled underpass during T5, *Grin1*$^{Y647S/+}$ mice were significantly slower than WT in reaching the goalbox (Tukey's post hoc test: $p = 0.0008$) **(Figure 7C)**. Despite atypical T5 performance, short- and long-term memory each appeared intact in variant mice, as latencies during repetition of the task 2 min (T6) and 24 h (T7) after initial exposure approached those of WT mice. Together, these results indicate that *Grin1*$^{Y647S/+}$ mice possess typical motivation to

reach the dark box and to encode and remember these trials but are initially slow to overcome novel obstacles impeding their travel.

DISCUSSION

Leveraging a newly developed mouse model alongside *in vitro* methods, this study of the Y647S variant reveals a complex phenotype ultimately driven by diminished NMDAR function. Variant NMDARs displayed increased sensitivity to endogenous agonists of the receptor in *Xenopus* oocytes, but >300-fold decreased NMDAR response amplitudes when expressed in mammalian cell lines and no detectable synaptic NMDAR function with *ex vivo* preparations from the hippocampus obtained from knock-in mice. To understand the pathogenic nature of this variant, we examined histological and behavioural features of the *Grin1*$^{Y647S/+}$ mice and found they displayed alterations in domains relevant to patient symptomology and to the broader characteristics of *GRIN1*-NDD. The present work reveals the complex manifestations of NMDAR variation underlying *GRIN1*-NDD and provides a representative whole-organism system to further probe pathological mechanisms and test novel therapies.

The Y647S variant imparts complex alterations to NMDAR expression and function

Our *in vitro* characterization of the Y647S variant revealed enhanced potency to co-agonists L-glutamate and glycine and mixed effects of the variant receptor to endogenous modulators, which were in some cases dependent on the expression of specific GluN2 subunits. The Y647S variant displayed decreased sensitivity to maximal inhibition by Zn^{2+}, increased sensitivity to Mg^{2+} when co-expressed with GluN2A and opposing levels of proton inhibition depending on the co-expressed GluN2 subunit. Interestingly, the complex profile of NMDAR sensitivity to agonists and endogenous modulators imparted by the Y647S variant was nearly identical to that reported for the p.Tyr647Cys (Y647C) variant [14, 22]. In both cases, structural modelling of the Y647S and Y647C variants found increased number of hydrogen bonds between the glycine ligand and the glycine-binding residues of the variant GluN1 compared to WT, offering a potential mechanism for the increased agonist affinity [14] which was also reported in the p.Tyr647His variant (numbered as p. Tyr668His) [44]. When expressed in HEK cells, Y647S variant NMDARs had dramatically reduced (>300-fold) current amplitude in response to application and rapid removal of agonists. This is due in part to reductions in channel opening probability and detectable cell-surface expression of Y647S variant NMDARs. This suggests that the structural changes imparted by the Y647S variant may stabilize a closed receptor state or increase the activation energy required for opening in addition to altering the trafficking of receptors to the plasma membrane, which has

been noted in previous studies [21,22]. Despite an increased *in vitro* sensitivity to agonists, the large reduction in surface expression of the Y647S variant NMDAR together with the reduced open probability will clearly reduce charge transfer mediated by variant NMDARs and thus likely accounts for the lack of observable currents, despite the inability to categorize the variant as loss of function by proposed *in vitro* criteria [17, 22].

Here, the *in vitro* trafficking deficits conferred by the Y647S variant are further elucidated in *ex vivo* hippocampal sections obtained from *Grin1*$^{Y647S/+}$ mice. Strikingly, brains from variant mice show a near-complete absence of NMDAR-mediated synaptic responses in CA1 pyramidal cells and a severe deficit in NMDAR-dependent long-term potentiation measured at the Schaffer-CA1 synapse. Despite this dramatic reduction of NMDAR function at this hippocampal synapse, GluN1 protein levels were found to be only modestly reduced in whole-brain homogenates from *Grin1*$^{Y647S/+}$mice and unaltered within the synaptic membrane fraction. Therefore, loss of NMDAR functionality does not appear to be driven by reductions in GluN1 abundance at the synaptic plasma membrane. A parsimonious explanation for this apparent discrepancy is that the profound reduction of open probability observed in heterologous systems may be even stronger in neurons, eliminating native currents despite near normal levels of protein. Alternatively, Fang et al. (2015) recently identified a mechanism by which regulated internalization of NMDARs not only reduced the number of receptors present on the cell surface, but also caused an inhibition of activity of the non-internalized NMDARs remaining on the surface mediated by increased serine phosphorylation [45]. This offers a potential explanation for the presence of NMDARs at the synaptic plasma membrane of *Grin1*$^{Y647S/+}$ mice that lack functionality. In these mice, NMDARs with two wildtype GluN1 subunits may properly deliver to the synaptic plasma membrane, while the NMDAR containing Y647S variant GluN1 may be removed from the membrane in response to dysfunction, thereby causing an inhibition of the activity of the NMDARs that remain on the surface membrane. Y647S variant-containing NMDARs undergoing internalization would be contained in endosomes, which are thought to be present in synaptic plasma membrane fractions [30, 46]. Future studies should examine the mechanisms underlying the preservation of relevant NMDAR protein levels at the membrane and the observed deficits in synaptic NMDAR functionality.

Grin1$^{Y647S/+}$ variant mice display early developmental and adult phenotypes reminiscent of clinical characteristics of _GRIN1_-NDD

We performed a phenotypic analysis of *Grin1*$^{Y647S/+}$ patient variant mice to determine if they displayed behavioural alterations in domains relevant to the symptomology seen in the patient harboring this variant and the broader clinical characteristics of *GRIN1*-NDD. In most cases, *GRIN1*-NDD is caused by a heterozygous de novo missense variant within the *GRIN1* gene [3], associated with clinical features including developmental delay or intellectual disability, alterations in speech, movement disorders, muscle tone abnormalities, epilepsy, and developmental malformation of cortex [3,14]. Indeed, the individual carrying the Y647S variant displayed seizure onset at 5 months, developmental delay, severe intellectual disability, hypotonia and cerebral atrophy with ventriculomegaly[2].

Hypotonia is seen in 66% of *GRIN1*-NDD patients, including the patient carrying the Y647S variant [2,3]. This symptom was studied by measuring righting reflex and wire hang time. The righting reflex in mice requires trunk control and is considered a standard test for the homologous labyrinthine function and body righting mechanisms observed in infants [47, 48]. In early development the righting reflex was found to be intact in *Grin1*$^{Y647S/+}$ pups, however, later in development *Grin1*$^{Y647S/+}$ variant mice displayed deficits in motor endurance in the wire hang task.

Changes to ultrasonic vocalizations (USVs), which are a form of vocal communication used by mice, were also observed [37]. Mouse models of NDDs frequently display alterations in USVs [37,49], with the increased rate of USV emissions seen in the *Grin1*$^{Y647S/+}$ variant mice pups likewise reported in a *GRIN2B* (*Grin2b*$^{C456Y/+}$) patient variant mouse model [50] and in mouse models of Rett syndrome [51] and Fragile X syndrome [52].

Interestingly, the motor deficits in the wire hang task that were identified in juvenile *Grin1*$^{Y647S/+}$ mice were not observed in adult mice, indicating that developmental delay in motor endurance ameliorated with age. However, several behavioural abnormalities were evident in adult mice including hyperlocomotion, increased sociability, reduced anxiety-like behaviours, and deficits in executive function.

Movement disorders in individuals with *GRIN1*-NDD often manifest as dystonia and hyperkinetic movements that are more similar to chorea rather than the manifestations of hyperactivity present in Attention-Deficit/Hyperactivity Disorder [3,53]. An endophenotype of hyperlocomotion is frequently observed in genetic mouse models with perturbations in NMDAR signaling [54]. When studying a specific *GRIN2A* (*Grin2a*$^{S644G/+}$) patient variant

mouse model, Amador et al. (2020) noted similar hyperactivity, which was not observed in the individual carrying that variant [33]. Rather than precisely recapitulating the human phenotype, altered locomotor activity could reflect a shared dysregulation of dopaminergic signaling caused by perturbation of NMDARs [13, 55, 56, 57].

The *Grin1*$^{Y647S/+}$ variant mice exhibit behaviours consistent with hypersociality, which has been previously identified in several related neurodevelopmental disorder mouse models including Williams Syndrome and Angelman Syndrome [58, 59, 60, 61]. When considered in conjunction with the reduced-anxiety phenotype of *Grin1*$^{Y647S/+}$ mice, increased sociability may be attributable to an impaired detection of danger which presents as social disinhibition [62]. In human patients, muted danger signals could present as social behaviours that are not appropriately modulated by context or level of familiarity with others, such as approaching or touching strangers [62, 63, 64].

The most striking endophenotype of *Grin1*$^{Y647S/+}$ mice, which recapitulates patient symptoms, is the increasing severity and frequency of spontaneous recurrent seizures when monitored weekly for 12 consecutive weeks. These seizures confer an important aspect of face validity to the *Grin1*$^{Y647S/+}$ mouse model, as the individual carrying this variant and ~65% of individuals with *GRIN1*-NDD present with epilepsy, which in two-thirds of cases is refractory to conventional antiseizure treatment [2,3]. Thus, the spontaneous nature of these seizures provides an opportunity to understand etiologically relevant mechanisms and to develop targeted treatments with greater potential efficacy than those of traditional antiepileptic drugs [65].

Neuroanatomical abnormalities have also been observed in *GRIN1*-NDD. Most common is a subtype of malformation of cortical development known as polymicrogyria [14], which is characterized by excessive cortical folds (gyri) associated with thinning or loss of cortical layers [66,67]. Polymicrogyria-associated *GRIN1* variants tend to cluster in the S2 segment of the ligand-binding domain or the M3 transmembrane domain of GluN1[14]. While the patient carrying the *GRIN1*$^{Y647S/+}$ variant presents with cerebral atrophy, polymicrogyria has not been identified [2]. However, this could be because neuroanatomical reports for this patient rely on CT scans, which cannot readily detect polymicrogyria [14]. Indeed, a patient carrying a substitution of cysteine for the tyrosine in the same location (p. Tyr647Cys; Y647C) displayed polymicrogyria detected with MRI [14]. Additionally, atypical hippocampal anatomy has been observed in patients with *GRIN1* variants, although more variably [3,14]. Here, the *Grin1*$^{Y647S/+}$ mouse was found to have normal neocortical thickness and cell counts, but abnormal hippocampal morphology. This pattern resembles the *Grin2a*$^{S644G/+}$ variant mouse line, which displays hippocampal thinning early in development but no changes to

neocortical lamination [33]. Other mouse models with NMDAR hypofunction have also been shown to express alterations to hippocampal volume with minimal differences in neocortical structure, despite NMDARs being highly expressed in this region [7, 68, 69]. Therefore, major neuroanatomical symptomology of the patient carrying the Y647S variant and those of broader *GRIN1*-NDD are recapitulated in this *Grin1*$^{Y647S/+}$ mouse model.

Significance of a *GRIN1*-NDD mouse model

Individuals diagnosed with *GRIN1*-NDD display debilitating symptoms including intellectual disability, muscular hypotonia, feeding difficulties, and epilepsy [3]. Current treatments focus on the management of symptoms; however, many patients are refractory to treatment, particularly those with epilepsy [3]. Thus, understanding how unique variants influence NMDAR function *in vivo* is crucial to advancing our understanding of *GRIN1*-NDD and the identification of targeted treatment strategies. The creation and characterization of the *Grin1*$^{Y647S/+}$ patient variant mouse, which recapitulates many key features of the clinical characteristics of the disorder, is a crucial step toward this goal. Importantly, the present study developed a regimen of weekly handling that reliably produces seizures in *Grin1*$^{Y647S/+}$ mice without the use of electrical kindling or convulsant drugs, providing an opportunity to understand etiologically relevant mechanisms underlying seizures and to test anti-seizure medications in future studies. Beyond this, the *Grin1*$^{Y647S/+}$ mouse model can be used to test gene-based treatments such as antisense oligonucleotide therapies or CRISPR-based gene editing, which have shown promise in the treatment of rare neurodevelopment disorders and rely on testing in animal models that closely mimic disease conditions [70]. Further, representative mouse models allow for the development of biomarkers, which if translatable to human patients provide a means of assessing disease pathology and treatment response in clinical trials [71].

Acknowledgement statement (including conflict of interest and funding sources):

We are grateful to acknowledge the work of Dr. Dawn E. Watkins-Chow and Dr. William J. Pavan from the National Human Genome Research Institute at the National Institutes of Health who created the *Grin1*$^{Y647S/+}$ mouse model. In addition, we are grateful to Dr. Alex W.M. Hooper and Dr. David R. Hampson from the Department of Pharmaceutical Sciences at the University of Toronto who provided use of the audiogenic seizure equipment utilized in this study. Further we are thankful to Dr. Lindsey Fiddes from the Microscopy Imaging Lab at the Faculty of Medicine, University of Toronto who assisted with microscopy and to Nicholas Wilson and Danielle Stevens who assisted with behavioural experiments

This work was supported by Canadian Institutes of Health Research (CIHR) Project Grant #169153, and grants from Simons Foundation Autism Research Initiative (SFARI) and CureGRIN Foundation to A.J.R., along with Ontario Graduate Scholarship and CIHR Canada Graduate Scholarships (CGS-M and CGS-D) awarded to M.T.S., by the NIH (NS111619 to S.F.T.; HD082373 and AG075444 to H.Y.), the CureGRIN Foundation to S.F.T., Austin's Purpose to S.F.T., and a grant from SFARI (732132 to S.F.T.). G.L.C. was supported by CIHR Foundation Grant #154276 and is the holder of the Krembil Family Chair in Alzheimer's Research.

As a member of the scientific advisory board (SAB) of the CureGRIN Foundation, A.J.R. has received financial renumeration. S.F.T. is a member of the SAB for Sage Therapeutics, Eumentis Therapeutics, Neurocrine, the GRIN2B Foundation, the CureGRIN Foundation, and CombinedBrain. S.F.T. is consultant for GRIN Therapeutics, a cofounder of NeurOp, Inc. and Agrithera, and a member of the Board of Directors for NeurOp Inc. S.F.T. is the PI on a research grant from GRIN Therapeutics to Emory. H.Y. is the PI on research grants from Sage Therapeutics and GRIN Therapeutics to Emory.

Data Availability

The data that support the findings of this study are available from the corresponding author upon reasonable request.

Author Contributions

M.T.S., P.T., Y.Y. K.I., W.C., Y.X., S.V., J.G., P.S.B.F., E.K.L., S.F.T., A.S., H.Y., G.L.C., and A.J.R. contributed to the conception and design of the study; M.T.S., P.T., Y.Y., K.I., W.C., Y.X., W.H., J.G., H.Y. and S.F.T. contributed to the acquisition and analysis of data; M.T.S., P.T., H.Y. contributed to the preparation of the figures; and M.T.S., P.T., Y.Y., K.I., W.C., Y.X., S.V., W.H., J.G., P.S.B.F., E.K.L., S.F.T., A.S., H.Y., G.L.C., and A.J.R. contributed to drafting of the text.

REFERENCES

1. Chen W, Shieh C, Swanger SA, et al. GRIN1 mutation associated with intellectual disability alters NMDA receptor trafficking and function. J Hum Genet 2017;DOI: 10.1038/jhg.2017.19.
2. Lemke JR, Geider K, Helbig KL, et al. Delineating the GRIN1 phenotypic spectrum: A distinct genetic NMDA receptor encephalopathy. Neurology 2016;DOI: 10.1212/WNL.0000000000002740.
3. Platzer K, Lemke JR. GRIN1-Related Neurodevelopmental Disorder. 2019 Jun 20 [Updated 2021 Apr 1]. In: Adam MP, Feldman J, Mirzaa GM, et al., editors. GeneReviews® [Internet]. Seattle (WA): University of Washington, Seattle; 1993-2024. Available from: https://www.ncbi.nlm.nih.gov/sites/books/NBK542807/
4. Paoletti P, Bellone C, Zhou Q. NMDA receptor subunit diversity: impact on receptor properties, synaptic plasticity and disease. Nat Rev Neurosci 2013;DOI: 10.1038/nrn3504.
5. Clements JD, Westbrook GL. Activation kinetics reveal the number of glutamate and glycine binding sites on the N-methyl-D-aspartate receptor. Neuron 1991; DOI: 10.1016/0896-6273(91)90373-8.
6. Kleckner NW, Dingledine R. Requirement for glycine in activation of NMDA-receptors expressed in Xenopus oocytes. Science. 1988; DOI: 10.1126/science.2841759.
7. Moriyoshi K, Masu M, Ishii T, et al. Molecular cloning and characterization of the rat NMDA receptor. Nature 1991;DOI: 10.1038/354031a0.
8. Johnson JW, Ascher P. Glycine potentiates the NMDA response in cultured mouse brain neurons. Nature 1987;DOI: 10.1038/325529a0.
9. Lerma J, Zukin RS, Bennett MV. Glycine decreases desensitization of N-methyl-D-aspartate (NMDA) receptors expressed in Xenopus oocytes and is required for NMDA responses. Proc Natl Acad Sci U S A 1990;DOI: 10.1073/pnas.87.6.2354.
10. Traynelis SF, Wollmuth LP, McBain CJ, et al. Glutamate receptor ion channels: structure, regulation, and function. Pharmacol Rev 2010;DOI: 10.1124/pr.109.002451.
11. Hansen, K.B., Wollmuth, L.P., Bowie, D., et al. Structure, Function, and Pharmacology of Glutamate Receptor Ion Channels. Pharmacol Rev 2021;DOI: 10.1124/pharmrev.120.000131.
12. Lemke JR. Predicting incidences of neurodevelopmental disorders. Brain 2020;DOI: 10.1093/brain/awaa079

13. Ohba C, Shiina M, Tohyama J, et al. GRIN1 mutations cause encephalopathy with infantile-onset epilepsy, and hyperkinetic and stereotyped movement disorders. Epilepsia 2015;DOI: 10.1111/epi.12987.
14. Fry AE, Fawcett KA, Zelnik N, et al. De novo mutations in GRIN1 cause extensive bilateral polymicrogyria. Brain 2018; DOI: 10.1093/brain/awx358.
15. Hamdan FF, Gauthier J, Araki Y, et al. Excess of de novo deleterious mutations in genes associated with glutamatergic systems in nonsyndromic intellectual disability. Am J Hum Genet 2011;DOI: 10.1016/j.ajhg.2011.02.001.
16. Brünger T, Pérez-Palma E, Montanucci L, et al. Conserved patterns across ion channels correlate with variant pathogenicity and clinical phenotypes. Brain 2023;DOI:10.1093/brain/awac305.
17. Myers SJ, Yuan H, Perszyk RE, et al. Classification of missense variants in the N-methyl-d-aspartate receptor GRIN gene family as gain- or loss-of-function. Hum Mol Genet 2023;DOI:10.1093/hmg/ddad104.
18. Benke TA, Park K, Krey I, et al. Clinical and therapeutic significance of genetic variation in the GRIN gene family encoding NMDARs. Neuropharmacology 2021;DO1:10.1016/j.neuropharm.2021.108805.
19. Murthy SE, Shogan T, Page JC, et al. Probing the activation sequence of NMDA receptors with lurcher mutations. J Gen Physiol 2012;DOI: 10.1085/jgp.201210786.
20. Kaniakova M, Krausova B, Vyklicky V, et al. Key amino acid residues within the third membrane domains of NR1 and NR2 subunits contribute to the regulation of the surface delivery of N-methyl-D-aspartate receptors. J Biol Chem 2012:DOI: 10.1074/jbc.M112.339085.
21. Kolcheva M, Kortus S, Krausova BH, et al. Specific pathogenic mutations in the M3 domain of the GluN1 subunit regulate the surface delivery and pharmacological sensitivity of NMDA receptors. Neuropharmacology 2021;DOI: 10.1016/j.neuropharm.2021.108528.
22. Xu Y, Song R, Perszyk RE et al. De novo GRIN variants in M3 helix associated with neurological disorders control channel gating of NMDA receptor. Cell Mol Life Sci 2024; DOI:10.1007/s00018-023-05069-z.
23. Chen W, Tankovic A, Burger PB, et al. Functional Evaluation of a De Novo *GRIN2A* Mutation Identified in a Patient with Profound Global Developmental Delay and Refractory Epilepsy. Mol Pharmacol 2017;DOI: 10.1124/mol.116.106781.

24. XiangWei W, Kannan V, Xu Y, et al. Heterogeneous clinical and functional features of GRIN2D-related developmental and epileptic encephalopathy. Brain 2019;DOI: 10.1093/brain/awz232.
25. Yuan H, Hansen KB, Zhang J, et al. Functional analysis of a de novo GRIN2A missense mutation associated with early-onset epileptic encephalopathy. Nat Commun 2014;DOI: 10.1038/ncomms4251.
26. Traynelis SF, Burgess MF, Zheng F, et al. Control of voltage-independent zinc inhibition of NMDA receptors by the NR1 subunit. J Neurosci 1998;DOI: 10.1523/JNEUROSCI.18-16-06163.1998.
27. Yuan H, Erreger K, Dravid SM, Traynelis SF. Conserved structural and functional control of N-methyl-D-aspartate receptor gating by transmembrane domain M3. J Biol Chem 2005;DOI: 10.1074/jbc.M414215200.
28. Hansen KB, Tajima N, Risgaard R, et al. Structural determinants of agonist efficacy at the glutamate binding site of N-methyl-D-aspartate receptors. Mol Pharmacol 2013;DOI: 10.1124/mol.113.085803
29. Swanger SA, Chen W, Wells G, et al. Mechanistic Insight into NMDA Receptor Dysregulation by Rare Variants in the GluN2A and GluN2B Agonist Binding Domains. Am J Hum Genet 2016;DOI: 10.1016/j.ajhg.2016.10.002.
30. Bermejo MK, Milenkovic M, Salahpour A, Ramsey AJ. Preparation of synaptic plasma membrane and postsynaptic density proteins using a discontinuous sucrose gradient. J Vis Exp 2014;DOI: 10.3791/51896.
31. Anderson WW, Collingridge GL. Capabilities of the WinLTP data acquisition program extending beyond basic LTP experimental functions. J Neurosci Methods 2007;DOI: 10.1016/j.jneumeth.2006.12.018.
32. Bankhead P, Loughrey MB, Fernández JA, et al. QuPath: Open source software for digital pathology image analysis. Sci Rep 2017;DOI: 10.1038/s41598-017-17204-5.
33. Amador A, Bostick CD, Olson H, et al. Modelling and treating GRIN2A developmental and epileptic encephalopathy in mice. Brain 2020;DOI: 10.1093/brain/awaa147.
34. Edwards CM, Small D, Bell T, et al. Early postnatal decabromodiphenyl ether exposure reduces thyroid hormone and astrocyte density in the juvenile mouse dentate gyrus. Physiol Behav 2020;DOI: 10.1016/j.physbeh.2020.112798.
35. Coffey KR, Marx RE, Neumaier JF. DeepSqueak: a deep learning-based system for detection and analysis of ultrasonic vocalizations. Neuropsychopharmacology 2019;DOI: 10.1038/s41386-018-0303-6.
36. Holy TE, Guo Z. Ultrasonic songs of male mice. PLoS Biol 2005;DOI: 10.1371/journal.pbio.0030386.

37. Premoli M, Pietropaolo S, Wöhr M, et al. Mouse and rat ultrasonic vocalizations in neuroscience and neuropharmacology: State of the art and future applications. Eur J Neurosci 2023;DOI: 10.1111/ejn.15957.
38. Bonetto A, Andersson DC, Waning DL. Assessment of muscle mass and strength in mice. Bonekey Rep 2015;DOI: 10.1038/bonekey.2015.101.
39. Kang W, Tong T, Park T. Corticotropin releasing factor-overexpressing mouse is a model of chronic stress-induced muscle atrophy. PLoS One 2020;DOI: 10.1371/journal.pone.0229048.
40. Wong H, Hooper AW, Kang HR, et al. CNS-dominant human FMRP isoform rescues seizures, fear, and sleep abnormalities in Fmr1-KO mice. JCI Insight 2023;DOI: 10.1172/jci.insight.169650.
41. Moy SS, Nadler JJ, Perez A, et al. Sociability and preference for social novelty in five inbred strains: an approach to assess autistic-like behavior in mice. Genes Brain Behav 2004; DOI:10.1111/j.1601-1848.2004.00076.x.
42. Ben Abdallah NM, Fuss J, Trusel M, et al. The puzzle box as a simple and efficient behavioral test for exploring impairments of general cognition and executive functions in mouse models of schizophrenia. Exp Neurol 2011;DOI: 10.1016/j.expneurol.2010.09.008.
43. Lam VM, Beerepoot P, Angers S, Salahpour A. A novel assay for measurement of membrane-protein surface expression using a β-lactamase. Traffic 2013;DOI: 10.1111/tra.12073.
44. Ragnarsson L, Zhang Z, Das SS, et al. GRIN1 variants associated with neurodevelopmental disorders reveal channel gating pathomechanisms. Epilepsia 2023; DOI:10.1111/epi.17776.
45. Fang XQ, Qiao H, Groveman BR, et al. Regulated internalization of NMDA receptors drives PKD1-mediated suppression of the activity of residual cell-surface NMDA receptors. Mol Brain 2015; DOI:10.1186/s13041-015-0167-1
46. Wu J, Petralia RS, Kurushima H et al. Arc/Arg3.1 regulates an endosomal pathway essential for activity-dependent β-amyloid generation. Cell 2011;DOI: 10.1016/j.cell.2011.09.036.
47. Feather-Schussler DN, Ferguson TS. A Battery of Motor Tests in a Neonatal Mouse Model of Cerebral Palsy. J Vis Exp 2016;DOI: 10.3791/53569.
48. Pellis SM, Pellis VC, Chen YC, et al. Recovery from axial apraxia in the lateral hypothalamic labyrinthectomized rat reveals three elements of contact-righting: cephalocaudal dominance, axial rotation, and distal limb action. Behav Brain Res 1989:DOI: 10.1016/s0166-4328(89)80144-5.

49. Scattoni ML, Crawley J, Ricceri L. Ultrasonic vocalizations: a tool for behavioural phenotyping of mouse models of neurodevelopmental disorders. Neurosci Biobehav Rev 2009:DOI:10.1016/j.neubiorev.2008.08.003.
50. Shin W, Kim K, Serraz B, et al. Early correction of synaptic long-term depression improves abnormal anxiety-like behavior in adult GluN2B-C456Y-mutant mice. PLoS Biol;DOI: 10.1371/journal.pbio.3000717.
51. Picker JD, Yang R, Ricceri L, Berger-Sweeney J. An altered neonatal behavioral phenotype in Mecp2 mutant mice. Neuroreport 2006;DOI: 10.1097/01.wnr.0000208995.38695.2f.
52. Lai JK, Sobala-Drozdowski M, Zhou L et al. Temporal and spectral differences in the ultrasonic vocalizations of fragile X knock out mice during postnatal development. Behav Brain Res 2014;DOI: 10.1016/j.bbr.2013.10.049.
53. Kuś J, Saramowicz K, Czerniawska M et al. Molecular Mechanisms Underlying NMDARs Dysfunction and Their Role in ADHD Pathogenesis. Int J Mol Sci 2023;DOI:10.3390/ijms241612983.
54. Mohn AR, Gainetdinov RR, Caron MG, Koller BH. Mice with reduced NMDA receptor expression display behaviors related to schizophrenia. Cell 1999;DOI: 10.1016/s0092-8674(00)81972-8.
55. Pei L, Lee FJ, Moszczynska A et al. Regulation of dopamine D1 receptor function by physical interaction with the NMDA receptors. J Neurosci 2004;DOI: 10.1523/JNEUROSCI.3922-03.2004.
56. Farsi Z, Nicolella A, Simmons SK et al. Brain-region-specific changes in neurons and glia and dysregulation of dopamine signaling in Grin2a mutant mice. Neuron 2023:DOI: 10.1016/j.neuron.2023.08.004.
57. Nakao K, Jeevakumar V, Jiang SZ et al. Schizophrenia-Like Dopamine Release Abnormalities in a Mouse Model of NMDA Receptor Hypofunction. Schizophr Bull 2019;DOI: 10.1093/schbul/sby003.
58. Feyder M, Karlsson RM, Mathur P et al. Association of mouse Dlg4 (PSD-95) gene deletion and human DLG4 gene variation with phenotypes relevant to autism spectrum disorders and Williams' syndrome. Am J Psychiatry 2010:DOI: 10.1176/appi.ajp.2010.10040484.
59. Toth M. The other side of the coin: Hypersociability. Genes Brain Behav 2019;DOI: 10.1111/gbb.12512.
60. Kozel BA, Barak B, Kim CA et al. Williams syndrome. Nat Rev Dis Primers. 2021; DOI:10.1038/s41572-021-00276-z.

61. Stoppel DC, Anderson MP. Hypersociability in the Angelman syndrome mouse model. Exp Neurol 2017;DOI:10.1016/j.expneurol.2017.04.002.
62. Wang HG, Bavley CC, Li A et al. Scn2a severe hypomorphic mutation decreases excitatory synaptic input and causes autism-associated behaviors. JCI Insight 2021;DOI:10.1172/jci.insight.150698.
63. Riby DM, Kirk H, Hanley M, Riby LM. Stranger danger awareness in Williams syndrome. J Intellect Disabil Res 2014;DOI:10.1111/jir.12055.
64. Richman DM, Dotson WH, Rose CA et al. Effects of Age on the Types and Severity of Excessive Fear or the Absence of Fear in Children and Young Adults With Autism. Journal of Mental Health Research in Intellectual Disabilities 2012;DOI:10.1080/19315864.2011.596614.
65. Löscher W. Critical review of current animal models of seizures and epilepsy used in the discovery and development of new antiepileptic drugs. Seizure 2011;DOI: 10.1016/j.seizure.2011.01.003.
66. Jansen AC, Robitaille Y, Honavar M et al. The histopathology of polymicrogyria: a series of 71 brain autopsy studies. Dev Med Child Neurol 2016;DOI:10.1111/dmcn.12840.
67. Squier W, Jansen A. Polymicrogyria: pathology, fetal origins and mechanisms. Acta Neuropathol Commun 2014;DOI:10.1186/s40478-014-0080-3.
68. Intson K, van Eede MC, Islam R et al. Progressive neuroanatomical changes caused by Grin1 loss-of-function mutation. Neurobiol Dis 2019;DOI: 10.1016/j.nbd.2019.104527.
69. Messersmith EK, Feller MB, Zhang H, Shatz CJ. Migration of neocortical neurons in the absence of functional NMDA receptors. Mol Cell Neurosci 1997;DOI: 10.1006/mcne.1997.0646.
70. Hong D, Iakoucheva LM. Therapeutic strategies for autism: targeting three levels of the central dogma of molecular biology. Transl Psychiatry 2023;DOI:10.1038/s41398-023-02356-y. Erratum in: Transl Psychiatry. 2023 Mar 7;13(1):80. doi: 10.1038/s41398-023-02386-6.
71. Wendler A, Wehling M. The translatability of animal models for clinical development: biomarkers and disease models. Curr Opin Pharmacol 2010; DOI: 10.1016/j.coph.2010.05.009.
72. Chou TH, Tajima N, Romero-Hernandez A, Furukawa H. Structural Basis of Functional Transitions in Mammalian NMDA Receptors. Cell 2020;DOI: 10.1016/j.cell.2020.05.052.

FIGURE LEGENDS

Figure 1. *GRIN1* p.Y647S variant alters *in vitro* NMDAR function. (A) The *GRIN1*-p.Y647S variant is located in M3 transmembrane domain (TMD), a critical element for channel gating. A homology model of the GluN1/GluN2A/GluN1/GluN2A receptor was built from previously published cryo-EM data for GluN1/GluN2B receptors [72]. **(B)** Composite concentration-response curves for glutamate (*left*; in the presence of 100 mM glycine) and glycine (*right*; in the presence of 100 μM glutamate) for WT GluN1 and GluN1-Y647S co-expressed with GluN2A by TEVC oocyte recordings (V_{HOLD} -40 mV). **(C)** Composite concentration-response curves for Mg^{2+} inhibition by TEVC oocyte recordings (V_{HOLD} -60 mV). **(D)** Composite concentration-response curves for Zn^{2+} inhibition by TEVC oocyte recordings (V_{HOLD} -20 mV). **(E)** Composite concentration-response curves for proton inhibition by TEVC oocyte recordings (V_{HOLD} -40 mV). *Right*: Summary of the effects of GluN1-Y647S variant on proton sensitivity, evaluated by the ratio of current response recorded at pH 6.8 to those recorded at pH 7.6. **(F)** Representative whole cell current responses recorded under voltage clamp (V_{HOLD} -60 mV) from transiently transfected HEK cells with WT GluN1/GluN2A and GluN1-Y647S/GluN2A NMDARs are shown in response to brief 5 ms application and rapid removal of 1 mM glutamate with 100 μM glycine present in all solutions. **(G)** Summary of current amplitude. **(H)** Summary of calculated channel open probability (P_{OPEN}) assessed by the degree of MTSEA potentiation by TEVC oocyte recordings (V_{HOLD} -40 mV). Data are expressed as mean ± SEM. * $p < 0.05$.

Figure 2: *Grin1* Y647S substitution and molecular characterization in a mouse model. (A) Sanger sequencing showing the A > C nucleotide mutation and diagnostic silent mutation from C > T in the preceding base pair in Y647S/+ mice. **(B)** Linear schematic representation of the GluN1 subunit, showing evolutionary conversation of amino acids between human and mouse and the site of mutation in the M3 transmembrane denoted with a circle and altered amino acid residue denoted with an asterisk. The tyrosine residue at position 647 is highly conserved across most of Vertebrata species and all four GluN2 subunits, indicating a potential critical role in channel function. ATD = amino terminal domain; CTD = carboxy terminal domain; M1-4 = transmembrane domains; agonist-binding domain (ABD) S1 and S2. **(C)** Reverse transcription PCR (RT-PCR) analysis of relative quantification of *Grin1*, *Grin2a* and *Grin2b* mRNA expression in forebrain normalized to housekeeping gene PGK1-2 (n=3-4) and +/+. **(D)** Western blot representation of total brain lysate and synaptic plasma membrane fractions probed for GluN1, GluN2A, GluN2B (n = 3). **(E)** Relative GluN1, GluN2A, and GluN2B protein in total brain lysate normalized to total protein stain and +/+ (n =3; p = 0.0361). **(F)** Relative GluN1, GluN2A and GluN2B protein in synaptic plasma membrane fractions normalized to total protein stain and +/+ (n =3). Data are expressed as mean ± SEM. *$p < 0.05$.

Figure 3: Adult *Grin1*$^{Y647S/+}$ mice display alterations in NMDAR-mediated synaptic transmission and long-term potentiation in the hippocampus. (A) Schematic of a hippocampal slice showing the positions of the stimulating and recording electrodes. CA3-CA1 fibre volley (FV; indicated by a grey arrow) and AMPA receptor-mediated fEPSPs (AMPAR-fEPSP) were recorded in standard ACSF (containing 1 mM Mg^{2+}) without channel blockers. NMDA receptor-mediated fEPSPs (NMDAR-fEPSP) were recorded in low (0.1 mM) Mg^{2+} ACSF with NBQX (10 μM) added to block AMPAR transmission. **(B)** Input/output (I/O) curves showing that increasing stimulus intensity corresponded to similar increases in FV amplitude in +/+ and Y647S/+ mice (left). The slope values of the linear regression fits (I/O slope) were not significantly different between genotypes, demonstrating largely unaltered presynaptic axon activation (right) (sexes combined: n = 12 +/+, n =12 Y647S/+). Representative traces shown above. **(C)** I/O curves showing the relationship between FV amplitude and AMPAR-fEPSP slope in +/+ and Y647S/+ mice (left). The I/O slopes were not significantly different between genotypes, indicating intact AMPAR-mediated synaptic transmission (right) (sexes combined: n = 12 +/+, n = 12 Y647S/+). Representative traces shown above. **(D)** Paired-pulse facilitation of AMPAR-fEPSPs measured across a range of inter-pulse intervals in +/+ and Y647S/+ mice (left). The paired-pulse ratio (PPR) at the 50 ms interval was not significantly different between genotypes, indicating no detectable differences in neurotransmitter release probability (right)

(sexes combined: n = 12 +/+, n = 12 Y647S/+). Representative traces for the 50 ms interval are shown above. **(E)** I/O curves showing the relationship between FV amplitude and NMDAR-fEPSP slope in +/+ and Y647S/+ mice (left). The I/O slope was significantly reduced in Y647S/+ mice, demonstrating deficiency in NMDAR-mediated synaptic transmission (right) (sexes combined: n = 6 +/+, n = 6 Y647S/+; $p < 0.0001$). **(F)** Time-course plot showing the change in AMPAR-fEPSP slope (plotted as % of baseline) following TBS in +/+ and Y647S/+ (left). Summary of the magnitude of LTP (% change from baseline) measured 80 – 90 min post TBS (right). LTP was significantly reduced in Y647S/+ mice (sexes combined: n = 6 +/+, n = 6 Y647S/+; $p < 0.0001$). Representative traces recorded before (1) and after (2) TBS are shown above. Error bars are ± SEM. Males and females are represented in circle and triangle symbols, respectively. ****$p < 0.0001$; ns: not significant.

Figure 4: Alterations to hippocampal morphology in adult *Grin1*$^{Y647S/+}$ mice. (A) Representative images of Nissl-stained brain sections with cortical thickness measurements and a 1.44 mm^2 region used for cortical cell counting in +/+ and Y647S/+ mice (scale bars = 1 mm). **(B)** Representative images of Nissl-stained neocortex in +/+ and Y647S/+ mice (scale bars = 100 μm). (**C)** Cortical thickness and (**D)** the number of cortical neurons were not significantly different between genotypes (sexes combined: n = 7 +/+, n = 4 Y647S/+). **(E)** Representative H&E images of the hippocampus proper, CA1, CA2 and dentate gyrus (DG) thickness measurements in +/+ and Y647S/+ mice (scale bars = 400 μm). **(F)** Y647S/+ mice displayed significantly reduced area of the pyramidal cell layer in the hippocampus proper (sexes combined: n = 8 +/+, n = 5 Y647S/+; $p = 0.0290$). **(G)** Trend toward decreased thickness of the hippocampus proper (sexes combined: n = 8 +/+, n = 5 Y647S/+, $p = 0.0874$), thickness measurements averaged between both hemispheres for each mouse. Data are expressed as mean ± SEM. *$p < 0.05$.

Figure 5: Early developmental phenotypes of *Grin1*$^{Y647S/+}$ mice. **(A)** At P6, righting reflex was not significantly different between genotypes (sexes combined: n = 38 +/+, n = 30 Y647S/+) **(B)** but Y647S/+ mice displayed significantly more ultrasonic vocalizations (USVs) in response to maternal isolation compared to +/+ mice (males n = 17 +/+, n = 17 Y647S/+, females n = 21 +/+, n = 13 Y647S/+, two-way ANOVA main effect of genotype: $F[1,64] = 8.891$; $p = 0.0046$). (**C)** At P21, Y647S/+ mice displayed significantly reduced bodyweight (sexes combined: n = 35 +/+, n = 29 Y647S/+, $p = 0.0383$). **(D)** and Y647S/+ exhibited significantly reduced holding impulse in the wire hang task (sexes combined: n = 30 +/+, n = 23 Y647S/+, $p = 0.0120$). Data are expressed as mean ± SEM. *$p < 0.05$; **$p < 0.01$. Males and females are represented in circle and triangle symbols, respectively.

Figure 6: Seizure and motor related behavioural phenotypes of adult *Grin1*$^{Y647S/+}$ mice. **(A)** Adult (12-22 weeks) bodyweight was significantly reduced in both sexes of Y647S/+ mice compared to +/+ (two-way ANOVA genotype × sex interaction: $F[1,83] = 9.430$, $p = 0.0029$; Tukey's post hoc tests: males n = 31 +/+, n =23 Y647S/+, $p = <0.0001$; females n = 20 +/+, n = 13 Y647S/+, $p = 0.0137$). **(B)** In adulthood, the holding impulse in the wire hang task was not significantly different between genotypes (males n= 31 +/+, n = 23 Y647S/+; females n = 20 +/+, n = 13 Y647S/+). (**C)** Y647S/+ mice had significantly increased total distance traveled in the open field test (sexes combined: n = 26 +/+, n = 19 Y647S/+, $p = 0.001$). **(D)** Distance traveled over time during the 2 hour open field test, with Y647S/+ mice travelling significantly greater distance in each 5-min bin from 5-25 and 35 min (two-way ANOVA genotype x time interaction: $F[23,989] = 16.65$, $p < 0.0001$; Tukey's post hoc tests: 5, $p < 0.0001$; 10, $p = 0.0013$; 15, $p = 0.0014$; 20, $p = 0.0012$; 25, $p = 0.0460$; 35, $p = 0.0281$) (sexes combined: n = 26 +/+, n = 19 Y647S/+). **(E)** The number of stereotypic behaviours engaged in during the open field test did not differ between genotypes (sexes combined: n = 26 +/+, n = 19 Y647S/+). **(F)** Percentage of +/+ and Y647S/+ (age 7-19 weeks at Week 1) displaying behavioural convulsions during behavioural convulsion tracking over 12 weeks (sexes combined: n = 17 +/+, n = 14 Y647S/+). (**G)** Representative photographs of each category of convulsion severity

observed during weekly handling as described in Table S1. **(H)** Heat map of convulsions severity observed in individual Y647S/+ mice over the course of 12 weeks. Data are expressed as mean ± SEM. *p < 0.05; **p < 0.01; ***p < 0.001; ****p < 0.0001. Males and females are represented in circle and triangle symbols, respectively.

Figure 7: Social and cognitive behavioural phenotypes of adult *Grin1*$^{Y647S/+}$ mice. (A) In the social interaction test, there was a statistically significant interaction between the effects of genotype and the type of stimulus (social or non-social) (two-way ANOVA genotype x stimulus interaction: F[1,46] = 13.36, p = 0.0007). Both genotypes spent significantly more time with the social stimulus than the non-social (Tukey's post hoc tests: +/+ p = 0.0159; Y647S/+ p< 0.0001) and Y647S/+ spent significantly less time with the non-social stimulus (p = 0.0169 sexes combined: n = 11 +/+, n = 14 Y647S/+). **(B)** Percentage of time spent in the open arms of the elevated plus maze was significantly increased in the Y647S/+ compared to +/+ (sexes combined: n = 18 +/+, n =16 Y647S/+, p <0.0001). **(C)** There was a statistically significant interaction between the effects of genotype and trial on the latency to reach the goal box (two-way ANOVA genotype x trial interaction: F[6, 138] = 4.310, p = 0.005). Y647S/+ mice displayed significantly greater latency to reach the goalbox on trial 5 where they were first presented with the digging challenge (Tukey's post hoc test: p = 0.008) (sexes combined: n = 13 +/+, n = 12 Y647S/+). Data are expressed as mean ± SEM. *p < 0.05; ***p < 0.001; ****p < 0.0001. Males and females are represented in circle and triangle symbols, respectively, except in Figure 6C.

TABLES

Table 1. Summary of the *in vitro* consequences caused by the *GRIN1*-p.Y647S variant

	co-expressed with GluN2A		co-expressed with GluN2B	
	WT GluN1	**GluN1-Y647S**	**WT GluN1**	**GluN1-Y647S**
Glu EC_{50}, μM (n)	3.2 [2.6, 4.1] (11)	0.074 [0.060, 0.090] (13)$	1.5 [1.1, 1.9] (9)	< 0.01 (12) $
Gly EC_{50}, μM (n)	1.2 [0.92, 1.5] (10)	0.036 [0.028, 0.047] (12)$	0.41 [0.30, 0.57] (6)	0.017 [0.012, 0.025] (13)$
%, $pH_{6.8}/pH_{7.6}$ [a]	42 ± 0.74 (21)	26 ± 0.66 (21) *	15 ± 0.70 (16)	21 ± 0.99 (8) *
H^+ IC_{50}, M (n)	1.01 E-07 (pH 7.0) (7-17)	6.55E-08 (pH 7.2) (7-15)	n.a.	n.a.
Zinc IC_{50}, nM (n) [b]	7.9 [5.8, 11] (8)	9.9 [8.5, 11] (6)	n.a.	n.a.
% inhibition at 300 nM zinc [b]	61 ± 3.3 (8)	47 ± 4.4 (6) *	n.a.	n.a.
Mg^{2+} IC_{50}, μM (n) [c]	22 [18, 27] (8)	12 [11, 14] (6) $	22 [16, 32] (6)	15 [10, 22] (12)
Amplitude, pA/pF	138 ± 31 (5)	0.29 ± 0.08 (6) *	49 ± 11 (5)	0.06 ± 0.03 (6) *
Calculated P_{OPEN}	0.28 ± 0.02 (8)	0.048 ± 0.005 (10) *	n.a.	n.a.
Surface/total ratio (beta-lac) [d]	1.0 (5)	0.16 ± 0.05 (5) *	1.0 (6)	0.44 ± 0.11 (6) *

The concentration-response curves for glutamate were obtained in the presence of 100 μM glycine, and the glycine concentration-response curves were determined in the presence of 100 μM glutamate. The concentration-response curves for Mg^{2+} were determined in the presence of 100 μM glutamate and glycine. Data shown are the mean EC_{50} or IC_{50} values with 95% confidence intervals determined from the $LogEC_{50}$ or $LogIC_{50}$ values; $ indicates 95% confidence intervals that are non-overlapping with corresponding WT GluN1/GluN2A- or GluN1/GluN2B-containing NMDARs. Data are mean ± SEM for current ratio at different pH values, percentage inhibition at 300 nM zinc, current amplitude, channel open probability (P_{OPEN}), and surface/total ratio of NMDAR expression, which were assessed by unpaired t-test (* $p < 0.05$); (*n*) is the number of cells recorded. *n.a.* indicates data not available. [a] percentage of the current at pH 6.8 compared to that at pH 7.6; [b] -20 mV of holding potential; [c] -60 mV of holding potential; [d] Part of the data from Xu et al., 2024 are included for comparison[22].

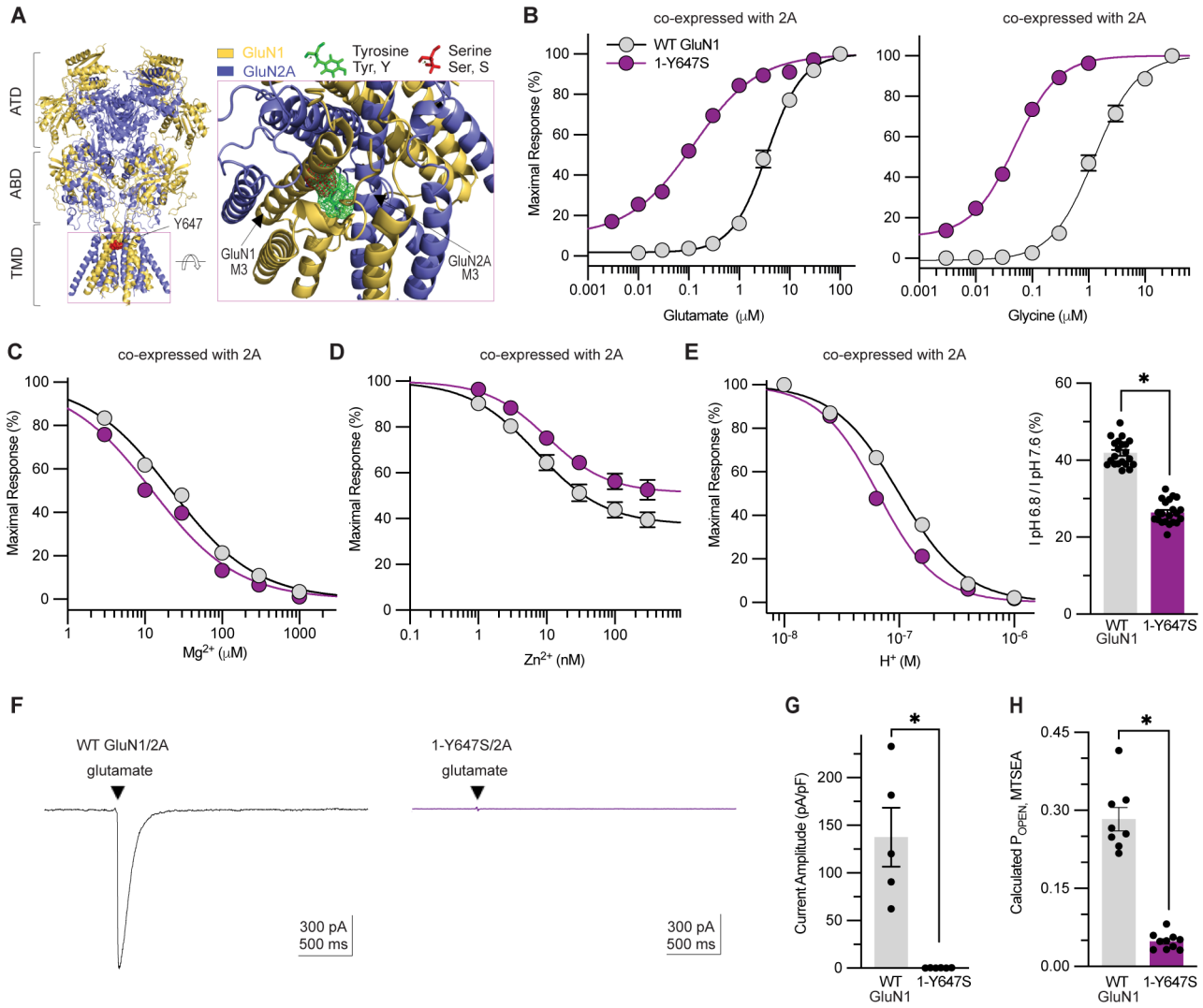
A
ATD
ABD
TMD
Y647
GluN1
GluN2A
Tyrosine
Tyr, Y
Serine
Ser, S
GluN1
M3
GluN2A
M3
B
co-expressed with 2A
WT GluN1
1-Y647S
Maximal Response (%)
Glutamate (μM)
co-expressed with 2A
Glycine (μM)
C
co-expressed with 2A
Maximal Response (%)
Mg2+ (μM)
D
co-expressed with 2A
Maximal Response (%)
Zn2+ (nM)
E
co-expressed with 2A
Maximal Response (%)
H+ (M)
I pH 6.8 / I pH 7.6 (%)
WT GluN1
1-Y647S
F
WT GluN1/2A
glutamate
300 pA
500 ms
1-Y647S/2A
glutamate
300 pA
500 ms
G
Current Amplitude (pA/pF)
WT GluN1
1-Y647S
H
Calculated POPEN, MTSEA
WT GluN1
1-Y647S

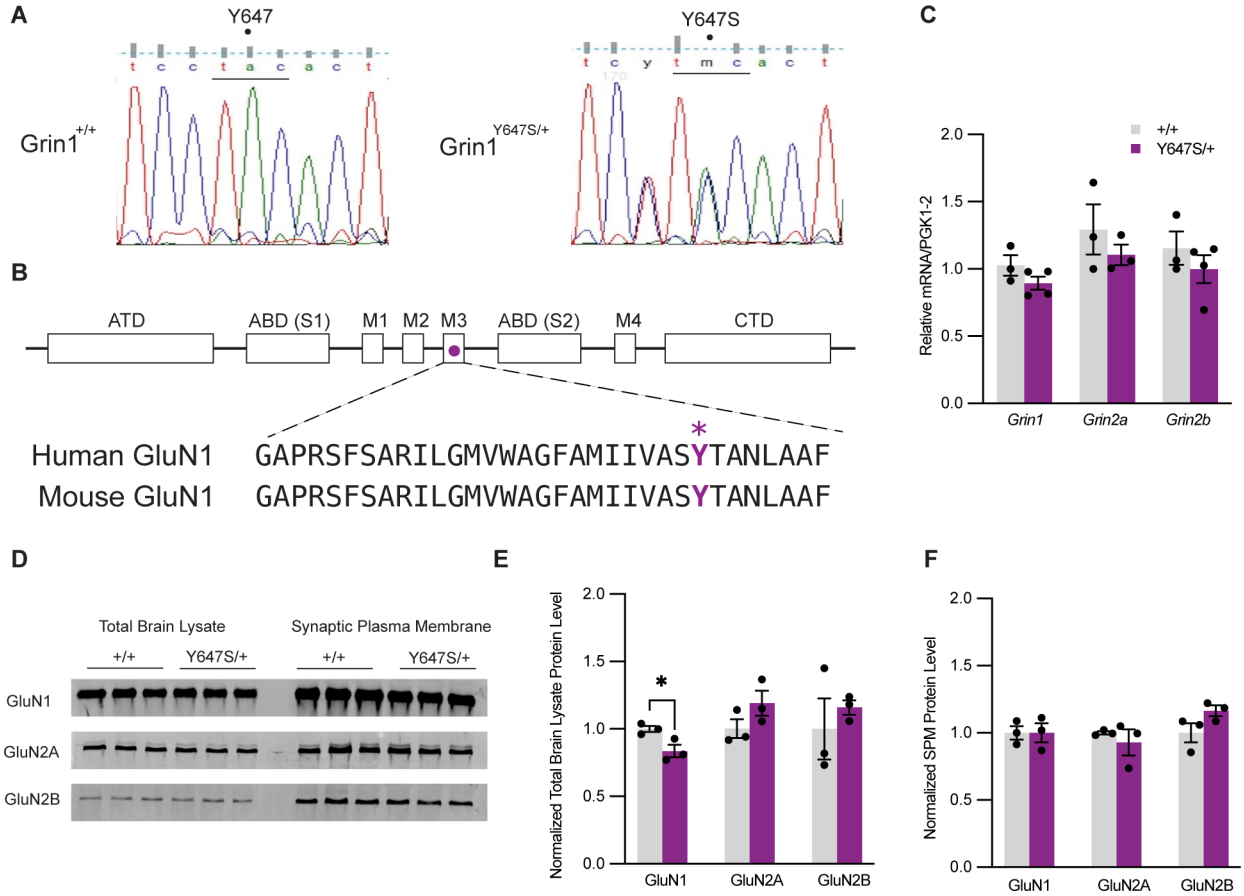
A
Y647
Grin1+/+
Y647S
Grin1Y647S/+
B
ATD
ABD (S1)
M1
M2
M3
ABD (S2)
M4
CTD
Human GluN1 GAPRSFSARILGMVWAGFAMIIVASYTANLAAF
Mouse GluN1 GAPRSFSARILGMVWAGFAMIIVASYTANLAAF
C
+/+
Y647S/+
Relative mRNA/PGK1-2
Grin1
Grin2a
Grin2b
D
Total Brain Lysate
Synaptic Plasma Membrane
+/+
Y647S/+
GluN1
GluN2A
GluN2B
E
Normalized Total Brain Lysate Protein Level
GluN1
GluN2A
GluN2B
F
Normalized SPM Protein Level
GluN1
GluN2A
GluN2B

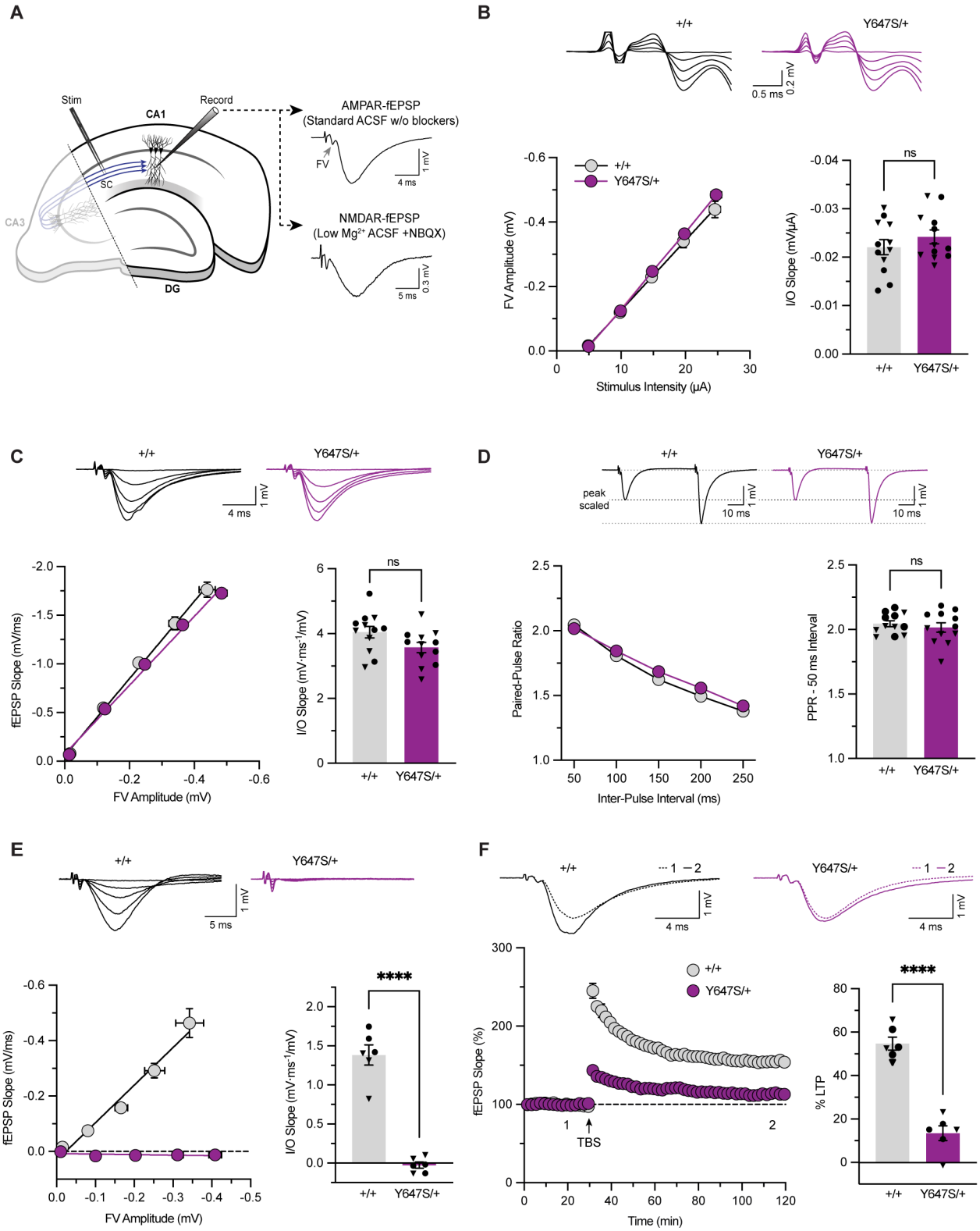
A
Stim
Record
CA1
SC
CA3
DG
AMPAR-fEPSP
(Standard ACSF w/o blockers)
FV
1 mV
4 ms
NMDAR-fEPSP
(Low Mg2+ ACSF +NBQX)
0.3 mV
5 ms
B
+/+
Y647S/+
0.5 ms
0.2 mV
FV Amplitude (mV)
Stimulus Intensity (μA)
I/O Slope (mV/μA)
ns
C
fEPSP Slope (mV/ms)
FV Amplitude (mV)
I/O Slope (mV·ms-1/mV)
D
peak
scaled
10 ms
Paired-Pulse Ratio
Inter-Pulse Interval (ms)
PPR - 50 ms Interval
E
5 ms
****
F
1
2
TBS
fEPSP Slope (%)
Time (min)
% LTP

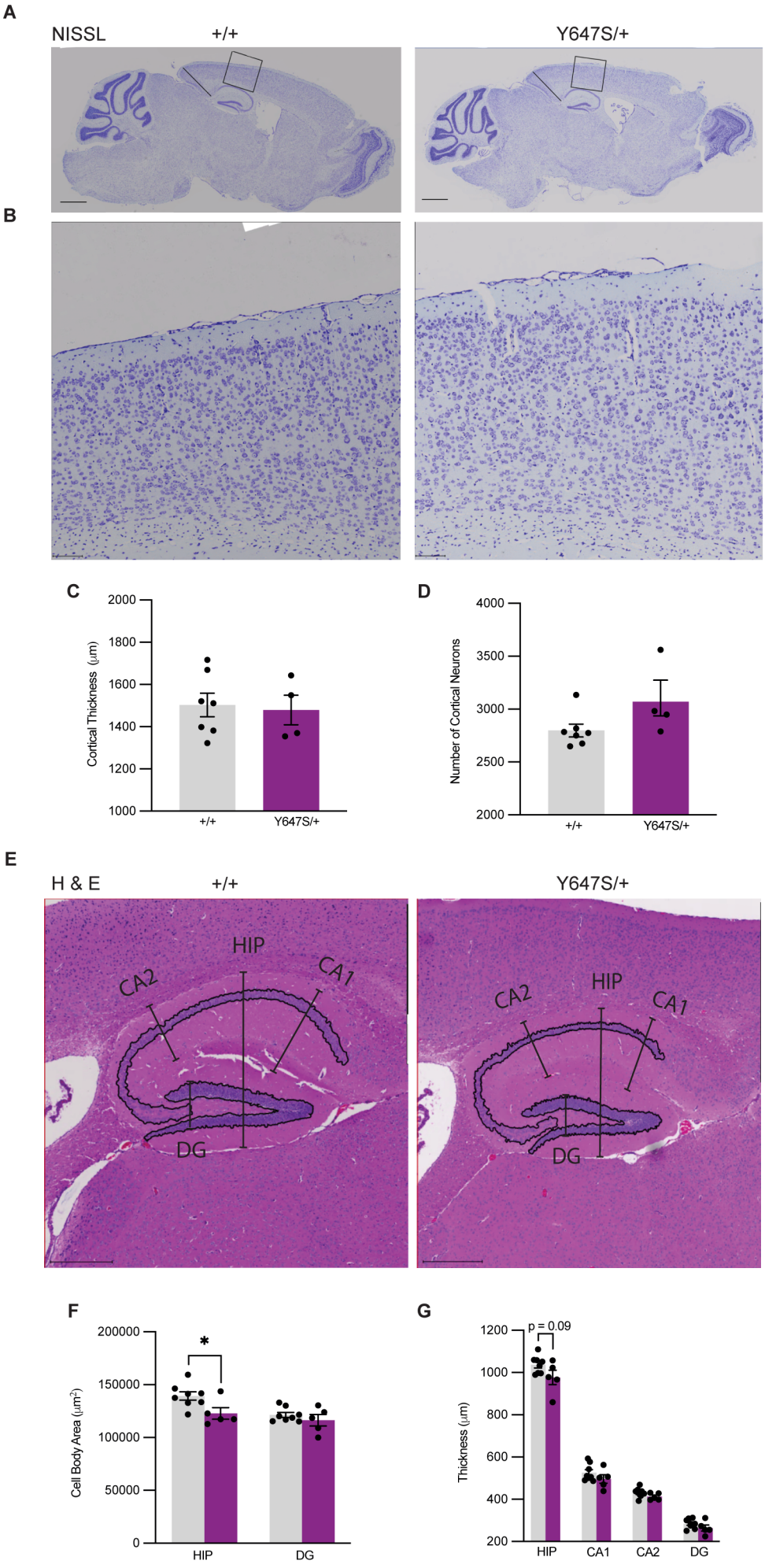
A
NISSL
+/+
Y647S/+
B
C
Cortical Thickness (μm)
2000
1800
1600
1400
1200
1000
+/+
Y647S/+
D
Number of Cortical Neurons
4000
3500
3000
2500
2000
+/+
Y647S/+
E
H & E
+/+
Y647S/+
HIP
CA2
CA1
DG
F
Cell Body Area (μm²)
200000
150000
100000
50000
0
*
HIP
DG
G
Thickness (μm)
1200
1000
800
600
400
200
p = 0.09
HIP
CA1
CA2
DG

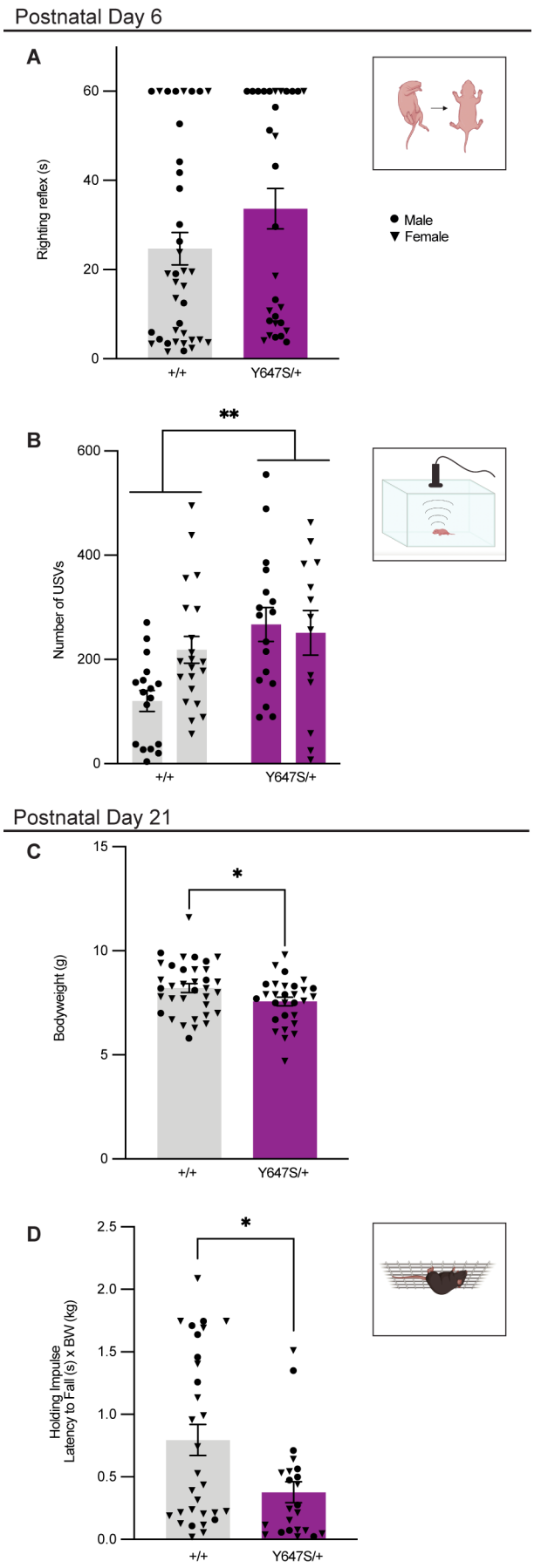
Postnatal Day 6
A
Righting reflex (s)
60
40
20
0
+/+
Y647S/+
Male
Female
B
**
Number of USVs
600
400
200
0
+/+
Y647S/+
Postnatal Day 21
C
*
Bodyweight (g)
15
10
5
0
+/+
Y647S/+
D
*
Holding Impulse
Latency to Fall (s) x BW (kg)
2.5
2.0
1.5
1.0
0.5
0.0
+/+
Y647S/+

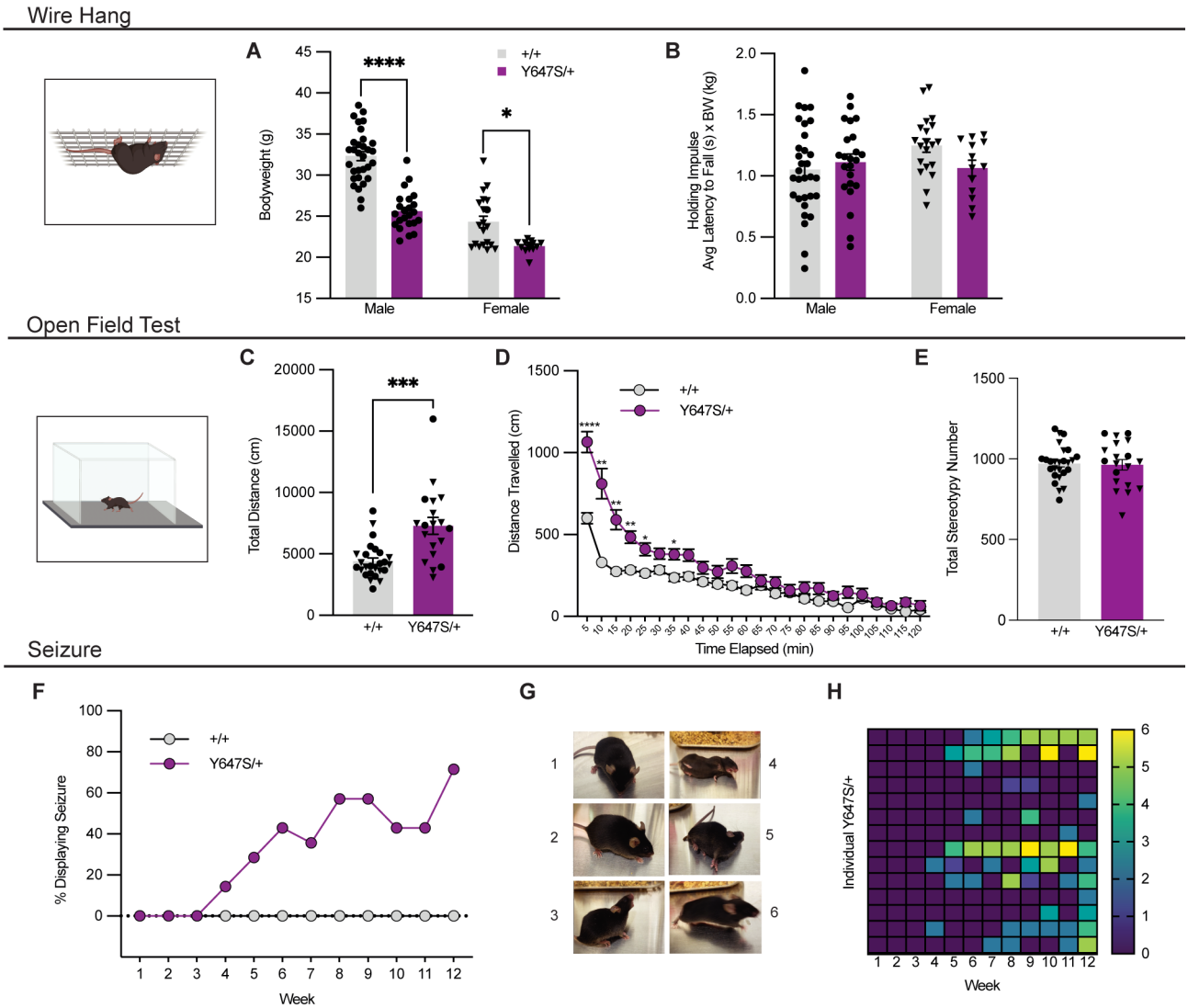
Wire Hang
A
Bodyweight (g)
45
40
35
30
25
20
15
****
*
+/+
Y647S/+
Male
Female
B
Holding Impulse
Avg Latency to Fall (s) x BW (kg)
2.0
1.5
1.0
0.5
0.0
Male
Female
Open Field Test
C
Total Distance (cm)
20000
15000
10000
5000
0
***
+/+
Y647S/+
D
Distance Travelled (cm)
1500
1000
500
0
+/+
Y647S/+
Time Elapsed (min)
E
Total Stereotypy Number
1500
1000
500
0
+/+
Y647S/+
Seizure
F
% Displaying Seizure
100
80
60
40
20
0
+/+
Y647S/+
1 2 3 4 5 6 7 8 9 10 11 12
Week
G
1
2
3
4
5
6
H
Individual Y647S/+
1 2 3 4 5 6 7 8 9 10 11 12
Week
6
5
4
3
2
1
0

Social Behaviour

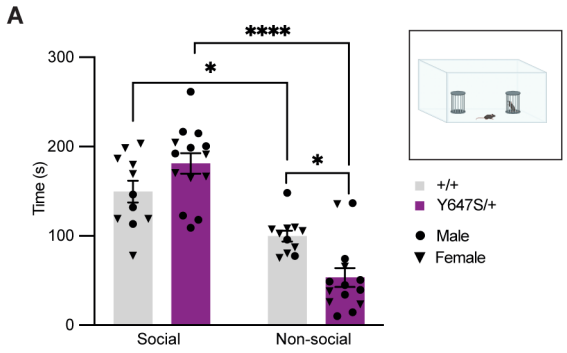

Elevated Plus Maze (Anxiety-Like Behaviour)

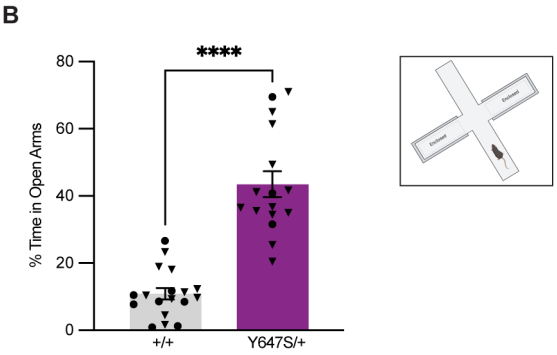

Puzzle Box (Executive Function)

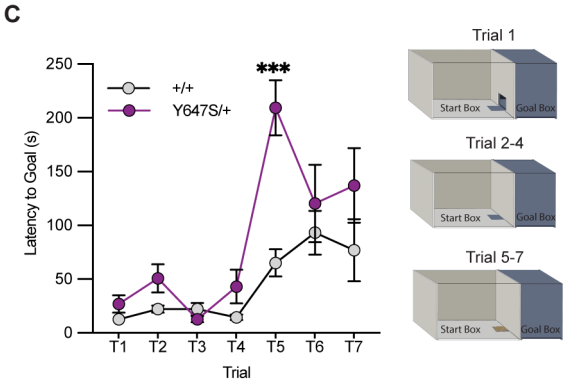

	Day 1			Day 2			Day 3
	T1	T2	T3	T4	T5	T6	T7
Door	Yes	No	No	No	No	No	No
Underpass	Open	Open	Open	Open	Sawdust	Sawdust	Sawdust